



HAL
open science

Intensification of Upper-Ocean Submesoscale Turbulence through Charney Baroclinic Instability

Xavier Capet, Guillaume Roulet, Patrice Klein, Guillaume Maze

► **To cite this version:**

Xavier Capet, Guillaume Roulet, Patrice Klein, Guillaume Maze. Intensification of Upper-Ocean Submesoscale Turbulence through Charney Baroclinic Instability. *Journal of Physical Oceanography*, 2016, 46, pp.3365 - 3384. 10.1175/JPO-D-16-0050.1 . hal-01455396

HAL Id: hal-01455396

<https://hal.science/hal-01455396>

Submitted on 7 Feb 2017

HAL is a multi-disciplinary open access archive for the deposit and dissemination of scientific research documents, whether they are published or not. The documents may come from teaching and research institutions in France or abroad, or from public or private research centers.

L'archive ouverte pluridisciplinaire **HAL**, est destinée au dépôt et à la diffusion de documents scientifiques de niveau recherche, publiés ou non, émanant des établissements d'enseignement et de recherche français ou étrangers, des laboratoires publics ou privés.

1 **Intensification of upper ocean submesoscale turbulence through Charney**
2 **baroclinic instability**

3 Xavier Capet*

4 *CNRS, IRD, Sorbonne Universités, UPMC, MNHN, LOCEAN, Paris, France*

5 Guillaume Rouillet, Patrice Klein and Guillaume Maze

6 *Univ. Brest, CNRS, IRD, Ifremer, Laboratoire d'Océanographie Physique et Spatiale (LOPS),*

7 *IUEM, Brest, France*

8 *Corresponding author address: LOCEAN, 4 place Jussieu, 75005 Paris, France.

9 E-mail: xclod@locean-ipsl.upmc.fr

ABSTRACT

10 This study focuses on the description of an oceanic variant of the Char-
11 ney baroclinic instability, arising from the joint presence of i) an equatorward
12 buoyancy gradient that extends from the surface into the ocean interior and
13 ii) reduced subsurface stratification, *e.g.*, as produced by wintertime convec-
14 tion or subduction. We analyze forced-dissipative simulations with and with-
15 out Charney baroclinic instability (C-BCI). In the former C-BCI strengthens
16 near-surface frontal activity with important consequences in terms of turbu-
17 lent statistics: increased variance of vertical vorticity and velocity, increased
18 vertical turbulent fluxes. Energetic consequences are explored. Despite the
19 atypical enhancement of submesoscale activity in the simulation subjected to
20 C-BCI and contrary to several recent studies the downscale energy flux at
21 submesoscale en route to dissipation remains modest in the flow energetic
22 equilibration. In particular, it is modest vis a vis the global energy input to the
23 system, the eddy kinetic energy input through conversion of available poten-
24 tial energy, and the classical inverse cascade of kinetic energy. Linear stability
25 analysis suggests that the southern flank of the Gulf Stream may be conducive
26 to oceanic Charney baroclinic instability in spring, following mode water for-
27 mation and upper ocean destratification.

28 **1. Introduction**

29 There has recently been a great interest in near-surface ocean turbulence properties in the length
30 scale range from a few hundreds of meters up to a few tens of kilometers. At these scales oceanic
31 flows exhibit frontal structures associated with significant deviations from geostrophy. This range
32 of turbulence scales (referred to as sub-mesoscale) is responsible, for transferring energy up to
33 larger scales (Sasaki et al. 2014), down to small scales (Capet et al. 2008c; Molemaker et al.
34 2010), for mediating air-sea interactions (Thomas and Taylor 2010) and perhaps contributing to
35 interior ocean mixing and the maintenance of the ocean thermohaline structure (D’Asaro et al.
36 2011). Submesoscale turbulence is also important through its associated vertical fluxes of proper-
37 ties between the near-surface and the interior, for example by contributing to the injection of deep
38 nutrients into the euphotic layer (Levy et al. 2001, 2012).

39 Recent studies suggest that a useful distinction exists between two different forms of upper
40 ocean submesoscale activity resulting from either stirring of surface buoyancy gradients by interior
41 mesoscale eddies (Nurser and Zhang 2000; Lapeyre et al. 2006; Thomas and Ferrari 2008) or from
42 the growth of mixed layer eddies and fronts through unstable processes (Fox-Kemper et al. 2008;
43 Fox-Kemper and Ferrari 2008; Mahadevan et al. 2010; Capet et al. 2008a; Mensa et al. 2013;
44 Skillingstad and Samelson 2012). The former is a consequence of baroclinic instability (BCI)
45 involving the ocean interior and leading to mesoscale turbulence that stirs the inhomogeneous
46 surface buoyancy field. This yields frontogenesis essentially around mesoscale eddies while other
47 parts of the ocean remain devoid of fronts. The latter arise when laterally heterogeneous boundary
48 layers subjected to sufficient destabilization by the atmosphere undergo mixed layer instability.
49 Mixed layer eddies exert a strong influence on the evolution of the boundary layer by contributing
50 to its rapid restratification, *e.g.*, following a mixing event. On the other hand they are considered

51 unimportant for the transport (advective or diffusive) of properties between the surface mixed layer
 52 and the ocean interior (Boccaletti et al. 2007; Capet et al. 2008b; Callies et al. 2016). Although
 53 typically less numerous the fronts associated with interior mesoscale activity are presumably more
 54 important for property exchanges between the surface and interior because their vertical extension
 55 is usually much larger than the height of the mixed layer (Ascani et al. 2013).

56 Schematically, two types of upper ocean frontal intensification may thus be associated with ei-
 57 ther: interior BCI having a near-surface frontogenetic expression because buoyancy gradients are
 58 present at the surface; or mixed layer BCI whose small horizontal length scale can be interpreted
 59 as resulting from weak near-surface stratification, hence a deformation radius of a few kilometers
 60 (Boccaletti et al. 2007). In practice the turbulent dynamics of the upper ocean is more complex
 61 though. One obvious reason is that both types of processes described above tend to coexist (Cal-
 62 lies et al. 2016; Capet et al. 2008d). A more original reason exposed in this study is that other
 63 baroclinic instability processes can exist that couple the unstable behaviors of the ocean surface
 64 and interior. Rouillet et al. (2012) consider a turbulent regime in which the primary instability
 65 arises from the joint presence of a surface buoyancy gradient and an interior velocity shear. This is
 66 the so-called Charney instability (Charney 1947) that is perhaps best understood with the help of
 67 the Charney-Stern necessary condition for baroclinic instability (Charney and Stern 1962). For a
 68 quasi-geostrophic (QG) zonal flow characterized by buoyancy anomaly, background Brunt-Väisälä
 69 frequency, and velocity field denoted respectively $b(y, z)$, N^2 and $U(y, z)$, the meridional gradient
 70 of QG potential vorticity is:

$$\partial_y Q = \beta - f \partial_z s_b + \frac{f^2}{N^2} \partial_z U \delta_0 - \frac{f^2}{N^2} \partial_z U \delta_{-H} \quad (1)$$

71 In (1) f is the Coriolis parameter, β is the planetary vorticity gradient, s_b is the slope of buoyancy
 72 surfaces ($s_b = -b_y/N^2$), H is the water depth assumed constant and δ is the Dirac delta function.

73 Relative vorticity has been neglected for simplicity. Surface and bottom boundary conditions for
74 buoyancy can be reexpressed in terms of infinitely thin sheets of a distinct potential vorticity form
75 (Bretherton 1966; Lapeyre and Klein 2006; Roulet et al. 2012), hence the Dirac delta functions in
76 (1).

77 A necessary and most frequently sufficient condition for BCI to develop is that $\partial_y Q$ changes sign
78 in the vertical. Phillips BCI arises from a sign change of interior PV first plus second rhs terms).
79 Eady BCI results from the fact that the third and fourth term (associated with upper and lower
80 interface PV sheets) are of opposite sign (Eady 1949; Molemaker et al. 2010). In its original at-
81 mospheric version Charney BCI corresponds to the situation where the stretching term is constant
82 and the sign reversal of Q_y occurs because $\beta - f\partial_z s_b$ and the lower PV sheet contribution are of
83 opposite signs. A variant situation more relevant to the upper ocean will be considered here where
84 the stretching term varies with depth and β is negligible. The *oceanic Charney baroclinic insta-*
85 *bility* (hereafter C-BCI) will refer to the unstable mode arising from the surface Dirac contribution
86 and underlying interior PV gradient ($\approx -\partial_z s_b$) having opposite signs.

87 In the ocean, situations conducive to C-BCI have been associated with negative s_b , *i.e.*, with
88 easterly flows as found on the equatorward flank of subtropical gyres (Tulloch et al. 2011; Gill
89 et al. 1974). There, the stretching term is expected to be negative while surface buoyancy decreas-
90 ing poleward is associated with a surface PV gradient that is positive. However, surface intensified
91 westerly currents with positive s_b can also be subject to C-BCI provided that the isopycnal tilt
92 s_b increases toward the surface. These are the conditions analyzed in Roulet et al. (2012). Vi-
93 sual inspection of the thermohaline structures shown in Klein et al. (2008a), Spall and Richards
94 (2000), Levy et al. (2001), Lima et al. (2002) and Akitomo (2010) indicates that process studies on
95 submesoscale dynamics make frequent implicit use of flow conditions characterized by $\partial_z s_b > 0$

96 and hence subjected to C-BCI (again, strictly speaking, the condition is $\partial_z s_b > \beta$ but β will be
97 negligible in practice as we justify below).

98 In the present study, our main goal is to gain insight into a submesoscale turbulent regime fueled
99 by C-BCI for an eastward flow, and in particular into its energetics. We compare two configura-
100 tions with the same degree of frontality but that differ in their upper ocean stratification so that
101 one has a mean state conducive to C-BCI while the other does not. A reference is provided by
102 a third setup that has no surface buoyancy gradient and whose turbulence is only due to interior
103 Phillips-like BCI (Pedlosky 1987; Lapeyre et al. 2006). The three setups are constructed so that
104 their differences are as limited as possible to facilitate their inter comparisons.

105 The paper is organized as follows. Methods are described in Section 2. Linear analyses of the
106 initial and equilibrated turbulent states are performed in Sec. 3. The simulations for the three
107 regimes and two numerical resolutions (eddy resolving with $\Delta x = 8$ km and submesoscale rich
108 with $\Delta x = 1$ km) are analyzed and compared in terms of turbulent statistics (Sec. 4) and ener-
109 getics (Sec. 5). The possibility that a finite depth surface mixed layer and its associated mixed
110 layer eddies disrupt C-BCI dynamics is subsequently investigated using one additional numerical
111 simulation (Sec. 6). We then explore the significance of the Charney BCI regime to the real ocean
112 based on in situ observations (Sec. 7). Some concluding remarks and perspectives are offered in
113 the final section.

114 **2. Methods**

115 *a. Setup designs*

116 In this study, the PE simulations for three baroclinic flows (S1,S2,S3) are analyzed and compared
117 at two different numerical resolutions, one typical of eddy resolving models ($\Delta x = 8$ km) and one

118 that is submesoscale rich ($\Delta x = 1$ km). In all cases the same computational domain is used: a
119 zonal reentrant channel that is 512 km long, 2040 km wide and 4000 m deep with flat bottom.

120 The three initial/reference buoyancy fields $b_{ref}(y, z)$ are constructed by connecting a dense north-
121 ern $b_N(z)$ and a light southern $b_S(z)$ buoyancy profile whose characteristics determine the setup
122 stratification and lateral buoyancy gradient. $b_N(z)$ and $b_S(z)$ are mathematically defined in ap-
123 pendix and shown in Fig. 1. The way $b_{ref}(y, z)$ is deduced from these profiles is as follows. Waters
124 within 200 km of the northern (resp. southern) boundary are homogeneous and have their buoy-
125 ancy equal to that of the dense (resp., light) profile. In the central part of the channel ($220 \text{ km} < y$
126 $< 1820 \text{ km}$) buoyancy goes smoothly from light to dense over a length scale $L_{jet} = 1600 \text{ km}$
127 with the frontal zone being concentrated in a $\sim 1000 \text{ km}$ central zone where the upper ocean value
128 of the lateral buoyancy gradient modulus (denoted M^2 hereafter) is $\sim 2 \times 10^{-8} \text{ s}^{-2}$ in S1 and S2
129 (see Fig. 1). The resulting upper ocean cross-front buoyancy structures are shown in Fig. 2. The
130 values of first baroclinic deformation radius obtained from domain-averaged N^2 are 29 km, 33 km
131 and 23 km respectively for S1, S2 and S3 (see also central profiles of Brunt-Väisälä frequency in
132 Fig. 1).

133 Overall, S2 corresponds to a more stratified upper ocean with $N^2 \approx 0.4-0.7 \times 10^{-4} \text{ s}^{-2}$ in the
134 upper 200 m (compared to $N^2 \approx 0.1-0.2 \times 10^{-4} \text{ s}^{-2}$ in S1) but note that the meridional buoyancy
135 gradient is the same at all depths in these two setups (Fig. 1c). As we will see below, the differences
136 in upper ocean N^2 lead to distinct instability properties for S1 and S2, with S1 being subjected to
137 C-BCI while S2 is not. Hydrographic observations presented in Sec. 7 suggest that S1 and S2
138 bear some resemblance with real ocean flow regimes. Meridional buoyancy gradients in S3 are
139 concentrated in the subsurface and vanish at surface. Lapeyre et al. (2006) analyze in details the
140 differences between two simulations that resemble S1 and S3. Our focus here is on the S1-S2
141 differences, although S3 occasionally provides a useful “no surface front” reference.

142 *b. Numerical framework*

143 PE numerical integrations are performed using the Regional Ocean Modeling System (ROMS)
144 configured for a β -plane at 45°N latitude ($f=1.0313\times 10^{-4}\text{ s}^{-1}$ and $\beta=1.6186\times 10^{-11}\text{ m}^{-1}\text{ s}^{-1}$).
145 The version of the code we use is the one referred to as UCLA-ROMS in Shchepetkin and
146 McWilliams (2009). For simplicity, only one prognostic state variable (buoyancy-like) is used.
147 The code uses a third-order upstream biased scheme for advection which provides lateral diffusiv-
148 ity/viscosity (Shchepetkin and McWilliams 1998, 2005). Baseline simulations use linear bottom
149 friction with a coefficient $r_d = 1.5 \times 10^{-3}\text{ m s}^{-1}$. Because the intensity of bottom drag is a key
150 parameter in the equilibration of baroclinic flows (Rivi re et al. 2004; Arbic and Flierl 2004) we
151 will also analyze a sensitivity run to the value of r_d . Simulation $S1_{r_d}$ is identical to S1 except that
152 it has $r_d = 1.5 \times 10^{-4}\text{ m s}^{-1}$, on the low end of commonly used linear bottom frictions.

153 Our main interest is in the statistical properties of their turbulence once a quasi-equilibrated
154 state is reached. Quasi-equilibrium is achieved by restoring zonally averaged and meridionally
155 smoothed buoyancy and zonal velocities toward their respective reference states. Thus, instabili-
156 ties growing out of the zonal mean flow can evolve without direct interference by the forcing. We
157 choose a restoring time scale equal to 50 days. Meridional smoothing is performed using a Han-
158 ning window of width 50 km which ensures that submesoscales are not directly forced (Roulet
159 et al. 2012).

160 Equilibrated solutions for the three setups S1-3 and at two different resolutions are presented in
161 this study: $\Delta x = 8\text{ km}$ and 40 levels ; $\Delta x = 1\text{ km}$ and 200 levels. These baseline simulations are
162 performed using a simple treatment of vertical mixing, which is possible because air-sea fluxes are
163 absent. Constant background vertical diffusion for buoyancy $\kappa_b^{(b)}$ and momentum $\kappa_b^{(u)}$ are applied
164 with values equal to respectively 10^{-5} and $10^{-4}\text{ m}^2\text{ s}^{-1}$. In addition, diffusion is enhanced locally

165 depending on the local Richardson number and occurrence of static instability, as described in
 166 Large et al. (1994). We note this contribution with a Ri subscript. The real ocean is generally
 167 overlaid by a well mixed layer in response to atmospheric forcing. In section 6, we test the im-
 168 portance of mixed layer dynamics and its interplay with Charney BCI. To do so, we artificially
 169 produce an upper ocean boundary layer in S1 and S2 by prescribing enhanced diffusion $\kappa^{(b)}$ and
 170 viscosity $\kappa^{(u)}$ above a level $z_{mld} = -65$ m. The simulations are respectively named S1_{ml} and S2_{ml}.
 171 Overall we thus have:

$$\kappa^{(b,u)} = \kappa_b^{(b,u)} + \kappa_{Ri}^{(b,u)} + \kappa_{mld}^{(b,u)}$$

172 with

$$\kappa_{mld}^{(b,u)} = 10^{-2} \left(1 - \tanh\left(\frac{z+5}{h_{trans}}\right) \right) \left(1 + \tanh\left(\frac{z-z_{mld}}{h_{trans}}\right) \right)$$

173 in S1_{ml} and S2_{ml} and 0 otherwise. Note that $\kappa_{mld}^{(b,u)}$ nearly vanish at the surface as observed in the
 174 ocean. For simplicity, the same vertical transition length scales h_{trans} is chosen equal to 10 m at
 175 the surface and bottom of the mixed layer.

176 *c. Experimental layout*

177 Analyses are carried out on equilibrated solutions without and with a mixed layer. The simula-
 178 tions are performed as follows. Initial zonal velocities are in geostrophic balance with the zonally
 179 invariant initial buoyancy field constructed as described above. Flow destabilization is triggered by
 180 a very small random perturbation added to the initial buoyancy field. The solutions are integrated
 181 over a four year period. For simplicity a year is assumed to last 360 days. The first three years are
 182 discarded as spin up because this is the time period required for eddy kinetic energy (EKE here-
 183 after; kinetic energy will be abbreviated as KE) to reach a plateau. The 36 model outputs stored
 184 every 10 days during the fourth year are used for analyses of the quasi-equilibrated solutions. At
 185 the end of the fourth year, near-surface vertical mixing is enhanced in S1 and S2 to create a mixed

186 layer and the simulation is pursued during 420 day. Interaction between the Charney baroclinic
 187 instability regime and mixed layer dynamics is evaluated over the last 360 days (36 outputs every
 188 10 days) in these simulation referred to as $S1_{ml}$ and $S2_{ml}$.

189 Simulation $S1_{rd}$ with reduced bottom drag is restarted from S1 instantaneous state after comple-
 190 tion of the 3 year spin up. It is further spun up for 6 months to let turbulence adjust and is analyzed
 191 over the subsequent year.

192 *d. Analysis framework*

193 We use and combine spatial and temporal forms of averaging to obtain statistical robustness. $\overline{\cdot}$
 194 refers to spatial averaging over the entire domain. Zonal invariance is key model symmetry. We
 195 will rely on zonal averaging denoted $\overline{\cdot}^{zo}$ to decompose the flow into mean and turbulent parts:
 196 $X(x, y, z) = \overline{X}^{zo}(y, z) + X'(x, y, z)$. Also, to increase statistical reliability, temporal averaging $\langle \cdot \rangle$
 197 can be performed over the 36 model outputs that are available for each simulation.

198 Combining these averaging operators, we define the root mean square (rms) of a variable X

$$X^{rms} = \langle \sqrt{\overline{X^2}} \rangle$$

199 and the standard deviation

$$X^{std} = \langle \sqrt{\overline{X'^2}} \rangle$$

200 The definition of eddy kinetic energy follows:

$$EKE = 1/2 \left[\overline{(u^{std})^2} + \overline{(v^{std})^2} \right].$$

201 where u and v are the zonal and meridional velocity components. The frontogenetic tendency
 202 presented in section 4 is defined as (Giordani and Caniaux 2001):

$$F_{sh} = - \left\langle \overline{(\partial_x \rho)^2 \partial_x u + (\partial_y \rho)^2 \partial_y v + \partial_x \rho \partial_y \rho (\partial_y u + \partial_x v)} \right\rangle,$$

203 where potential density ρ is related to buoyancy by $b = -\frac{g}{\rho_0}\rho$, with ρ_0 a reference density that we
204 choose equal to 1000 kg m^{-3} .

205 Our model outputs are 10 days apart which is not long enough to consider them independent
206 realizations. We find that mesoscale energy levels tend to fluctuate on time scales from weeks to a
207 few months (fluctuations on longer scales are also present albeit with reduced amplitude). When
208 computing uncertainty we will assume that our 360 days runs correspond to only 12 independent
209 realizations, hence uncertainty on estimates of $\langle \bar{X} \rangle$ will be $1/\sqrt{12} X^{std}$. However we note that
210 our analyses are for equilibrated solutions with very limited drift in energy between start and end
211 states, so that fluxes presented in Sec. 5 closely balance each other.

212 3. Linear analysis

213 Linear stability analysis is performed to characterize the unstable modes of the three setups. The
214 method follows Roulet et al. (2012) with a linearization of the QG equations about the reference
215 states. Relative vorticity is neglected. The key inputs are the northern and southern density profiles
216 and width of the baroclinic zone. Linear stability of the equilibrated states produced by model
217 integrations and presented in details in the next section are also analyzed. To do so, time- and
218 zonal-mean density profiles 250 km north and south of the jet axis (at $y=1000 \text{ km}$) are used.
219 Results for a shorter across-jet distance are not significantly different. Growth rates are strongly
220 reduced for northern and southern density profiles taken at the extreme ends of the domain but
221 they do not reflect, in this case, the turbulent behavior of the most energetic region near the jet
222 axis.

223 Results in terms of growth rate and vertical structure of the most unstable modes are shown
224 in Fig. 3. The quantity $IQ_y = \int_{-H}^z \partial_y Q dz$, where $\partial_y Q$ is given in (1), is also shown for the ini-
225 tial/reference and model equilibrated states to connect instability modes with the Charney-Stern

226 theorem. Vertically integrating $\partial_y Q$ allows us to explicitly represent the Dirac contribution associ-
227 ated with the surface PV sheet. Note that sign changes of the meridional PV gradient correspond
228 to extrema for its vertical integral (represented with open circles in Fig. 3). Below 500 m depth
229 all setups have similar IQ_y profiles with the extremum around 1000 m being responsible for the
230 low wavenumber unstable mode (e-folding time scale around 20 days, wavelength of the order of
231 200 km, *i.e.*, ≈ 5 -6 deformation radii). In addition, S1 initial state possesses a prominent shorter
232 mode with a most unstable wavelength at about 18km (associated e-folding time scale is 12 days).
233 Eigenvector's modulus reveal the contrasted nature of the low and high wavenumber modes. The
234 former corresponds to the gravest baroclinic mode, with a unique zero-crossing of the real and
235 complex parts of the eigenvectors about 1000 m depth (not shown). The latter is strongly surface
236 trapped with negligible signature below 400-500 m depth. It results from the presence of an IQ_y
237 minimum below the surface and a prominent discontinuity at the surface induced by the Dirac den-
238 sity contribution. This unstable mode is similar in essence to the Charney mode (Charney 1947).
239 Note that in the upper 1500 m, IQ_y changes with depth due to vortex stretching systematically
240 dominate over the β contribution.

241 The precise choice of some parameters used in the construction of the initial states can now be
242 more easily justified. In particular, the finite δb_s value chosen for S2 (see appendix and Table 2)
243 corresponds to the minimal amount of surface stratification that needs to be added to S1 buoyancy
244 profiles to make IQ_y monotonic above 1000 m depth, thereby suppressing the high wavenumber
245 Charney mode.

246 Anticipating on Sec. 4 we present the linear instability analysis performed on the mean turbulent
247 states obtained in our numerical simulations, *i.e.*, on states rectified by turbulent fluxes. Results
248 indicate that flow turbulence affects the low wavenumber interior modes significantly less than the
249 Charney mode of S1 which is strongly modified by turbulent rectification (maximum growth rate

250 reduced by 40 % and significant shift of the corresponding most unstable wavenumber; compare
 251 gray and black curves in Fig. 3b). In agreement with the nonlinear results we present below and
 252 also the conclusions of Roulet et al. (2012) we attribute this to the efficiency with which the
 253 Charney mode converts available potential energy (APE) into EKE, thereby producing an intense
 254 near-surface restratification that reverses the sign of Q_y in the upper 70-80 m and regularizes the
 255 near-surface behavior of IQ_y (compare the near surface structure of IQ_y for the basic and model
 256 mean states in Fig. 3a). This near-surface sign reversal of Q_y means that modes with short enough
 257 vertical/horizontal scales are no longer unstable because Q_y is one-signed in their depth range of
 258 influence. A short wave cut off is indeed present for the S1 nonlinear state (see Fig. 3b) while it is
 259 absent for the reference state, as in the original Charney problem (Charney 1947; Pedlosky 1987).

260 4. Turbulence properties in quasi-equilibrium

261 The differences between the solutions for the three setups in terms of eddy kinetic energy, verti-
 262 cal velocity rms, vertical eddy flux of buoyancy and frontogenetic tendency are revealed in Figs. 4
 263 and 5 for two resolutions typical of eddy-resolving ($\Delta x = 8$ km, 50 vertical levels) and subme-
 264 soscale rich ($\Delta x = 1$ km, 200 vertical levels) simulations.

265 Mesoscale resolving solutions exhibit limited differences in terms of relative vorticity (Figs. 4
 266 a-c at the surface) and w'^{rms} depth distribution (fig. 5d) despite a noticeable signature of upper
 267 ocean surface frontogenesis in S1, S2 above ~ 500 m depth (see Fig. 5h). Effects of frontogenesis
 268 on domain-averaged vertical buoyancy flux are also limited although less so than for w'^{rms} . Com-
 269 parison of S1 and S2 reveals that Charney BCI brings only modest differences, most noticeably
 270 for $\langle \overline{w'b'} \rangle$ above 200m depth (compare S1 and S2 profiles in Fig. 5f).

271 Because the fine scales are energized by near-surface frontogenesis present in S1-2 and by high
 272 wavenumber Charney instability in S1, the solution most (respectively, least) affected by the res-

273 olution increase is S1 (resp. S3). In S1, a dramatic change with resolution is the emergence of a
 274 well marked $\langle \overline{w'b'} \rangle$ maximum at 100 m depth for $\Delta x = 1$ km. At that depth $\langle \overline{w'b'} \rangle$ increases
 275 4-fold compared to $\Delta x = 8$ km. The $\langle \overline{w'b'} \rangle$ near-surface increase with resolution in S2 is more
 276 limited (about two-fold). By construction, the basic states of S1 and S2 have identical meridional
 277 buoyancy gradients and we have verified that this is also the case for their rectified mean states.
 278 Their eddy kinetic energy is also very similar (Fig. 5a). Therefore near surface frontogenesis re-
 279 sulting from the stirring of mean buoyancy gradients by mesoscale activity has no reason to differ.
 280 The difference in w^{rms} and $\langle \overline{w'b'} \rangle$ thus arises from the expression of the Charney mode in S1
 281 when resolution allows it. Between 0 and 300 m depth, *i.e.*, roughly the ocean layer where the PV
 282 meridional gradient is negative in S1 (see Fig. 3a) the Charney mode is thus associated with over
 283 60 % of the vertical buoyancy flux, provided resolution is fine enough to permit the representa-
 284 tion of fine scale instabilities (and their nonlinear consequences). As noted in Sec. 3 this flux has
 285 important consequences in terms of instability of the mean rectified state.

286 The visual aspect of the instantaneous relative vorticity and w fields is in agreement with the
 287 statistical description. In S2, frontogenesis manifests itself through the intensification of a limited
 288 number of fine-scale filamentous structures mainly located in between mesoscale eddies. Thus
 289 the typical submesoscale features in S2 are fronts and filaments whose alongfront length scale
 290 seems of the order of 100 km or more, *i.e.*, indicative of mesoscale stirring. In contrast, in S1
 291 the central part of the computation domain is more densely populated with submesoscale features:
 292 numerous submesoscale eddies with diameters less than 20 km and a marked cyclonic preference
 293 (Munk et al. 2000); fronts/filaments broken up or undulating with associated length scales of tens
 294 rather than hundreds of kilometers. The S1/S2 differences are most evident at the surface but they
 295 are still noticeable at 110 m depth, where S1 has its $\langle \overline{w'b'} \rangle$ maximum and the linear Charney

296 mode is still quite influential (Fig. 3b inset). Vertical velocity fields at 110 m also exhibit similar
297 differences, S1 vertical velocities being richer in fine-scale structures.

298 For S3, increased resolution helps better resolve vorticity filamentation arising from stirring by
299 interior mesoscale activity (compare Figs. 4c and f). However, no surface intensification occurs
300 owing to homogeneous surface buoyancy. Note though the significant enhancement of the deep
301 vertical buoyancy flux maximum when going from 8 to 1 km resolution (compare Fig 5e and f).
302 This surprising result is further discussed in the final section.

303 **5. Energetics**

304 In this section we investigate how the solutions energetically equilibrate. Our main focus is
305 the strength of the downscale kinetic energy transfer due to advection. The importance of such
306 downward energy transfers in the overall equilibration of the ocean is debated (Capet et al. 2008c;
307 Klein et al. 2008a; Molemaker et al. 2010; Marchesiello et al. 2011; Pouquet and Marino 2013;
308 Barkan et al. 2015). One issue is that the studies with the largest downscale KE transfers are those
309 for idealized flows whose relevance to the ocean are unclear, in particular because they do not
310 have upper ocean intensified stratification. On the other hand, realistic flows tend to have limited
311 or negligible forward cascades of KE. We see S1 as a good candidate to maximize the importance
312 of the downscale KE flux (given the intensity of its submesoscale frontal activity) while remaining
313 close to realistic ocean conditions.

314 We start by examining the 2D horizontal velocity spectra computed as in Capet et al. (2008c)
315 except that no procedure is applied to periodize the fields because our reentrant channel setup im-
316 plies periodicity in the x direction by construction while the weakness of the flow near the northern
317 and southern walls makes the issue of periodicity in the y direction irrelevant (tapering in the y
318 direction does not affect our results, not shown). Power spectrum densities for surface horizontal

319 velocities (Fig. 6) are generally consistent with an energization of submesoscale turbulence by
 320 both C-BCI, and general stirring of the surface buoyancy field. S1 has the shallowest surface EKE
 321 spectrum which roughly follows a $-5/3$ power law¹ (Fig. 6) whereas the spectral slope of S3 is
 322 ~ -3 to -3.5 , as expected for interior QG turbulence. S2 spectral slope is intermediate. Spectra
 323 for S3 at the surface and 110 m depth are not significantly different given estimate uncertainty
 324 (computed from the spectrum variance between model outputs, not shown) and neither are 110m
 325 depth spectra for S2 and S3 in the range $k \gtrsim 8 \times 10^{-5} \text{ rad m}^{-1}$. As discussed in, *e.g.*, Klein et al.
 326 (2008a) S2 energization by surface dynamics is progressively restricted to smaller wavenumbers
 327 with increasing depth. S1 EKE level at 110 m depth is still significantly higher than in S2 for k
 328 $\gtrsim 10^{-4} \text{ rad m}^{-1}$ which is roughly consistent with the range of influence of the Charney mode as
 329 determined from the linear stability analysis. Nevertheless S1 also exhibits a similar steepening
 330 of its KE spectrum as depth increases, even well within the range of influence of the C-BCI mode
 331 (*e.g.*, at 110 m). We interpret this tendency as a combination of reduced frontogenetic efficiency
 332 with depth (also felt by S2, see Fig. 5h) and reduced energization of the submesoscale flow by
 333 C-BCI (see the eigenvector vertical structure shown in Fig. 3b from the linear analysis).

334 Underlying these differences in EKE spectrum are major differences in APE to EKE conversion
 335 $\langle \overline{w'b'} \rangle$ as already noticed (see Fig. 5c for their overall magnitude). To better rationalize the
 336 behavior of EKE as a function of depth we find useful to examine the fraction of APE to EKE
 337 conversion $C(z) = \langle \overline{w'b'} \rangle$ that takes place in the submesoscale range. Fig. 7 represents the ratio
 338 C^{sm}/C as a function of depth, where

$$C^{sm}(z) = \langle \int_{k > k^{sm}} \Re e \left[\widehat{w}^* \widehat{b} \right] dk \rangle, \quad (2)$$

¹This energy distribution should not be mistakenly interpreted as the consequence of an inertial range for surface KE energy. To the contrary it is an additional KE input into the submesoscale range that is responsible for the difference between S1 and S2 power spectra. Both spectra reflect a complex balance between nonlinear fluxes scales and sinks/source terms that are active over the entire wavenumber range.

339 the caret is a horizontal 2D Fourier transform, the symbol \mathcal{Re} denotes the operator that selects the
 340 real part and wavenumber integration is done in k shells ($k = |\mathbf{k}_h|$ is the horizontal wavenumber).
 341 We choose $k^{sm} = 3 \times 10^{-4} \text{ rad m}^{-1}$ (20 km wavelength) and note that this value corresponds
 342 approximately to the maximum unstable wavenumber for the C-BCI mode in S1 (see Fig. 3b).
 343 It is also the lower bound of the wavenumber range where a downscale EKE flux is found in
 344 S1 as we will see below. For both S1 and S2 C^{sm}/C is maximum at the surface and decreases
 345 rapidly with depth. A factor 2 to 3 reduction is found at 20 m depth in S1 (the reduction is even
 346 more abrupt in S2). We interpret this rapid decrease as a consequence of reduced frontogenetic
 347 efficiency with depth (also felt by S2, see Fig. 5h) while the depth dependance of the amplitude
 348 of the C-BCI linear mode would predict a much gentler reduction with depth (see the eigenvector
 349 vertical structure in Fig. 3b).

350 The near-surface confinement of submesoscale energization in S1 (and even more so in S2)
 351 has important implications for the flow dissipation. In the remainder of this section, we present
 352 some analyses suggesting that, even in the submesoscale energized S1, downward KE transfers
 353 (by advection) are of limited significance in terms of flow equilibration. Spectral EKE transfer are
 354 estimated as (Capet et al. 2008c):

$$\Sigma_{\Pi}(k) = - \left\langle \int_{z=-200m}^0 \int_k^{k_{\max}} \mathcal{Re} \left[\widehat{\mathbf{u}}_h^* \cdot (\widehat{\mathbf{u}_h \cdot \mathbf{r}}) \widehat{\mathbf{u}}_h \right] dk dz \right\rangle \quad (3)$$

355 where \mathbf{u}_h is the instantaneous horizontal velocity vector field and temporal averaging over the 36
 356 model outputs is performed. Although the precise value (- 200 m) is arbitrary the bottom of the
 357 integration depth range is chosen so as to evaluate the strength of the downscale KE flux in a layer
 358 that is rich in submesoscale but also sufficiently thick to be of some significance (as opposed to a
 359 layer of a few tens of meters, *i.e.*, the typical width of oceanic surface boundary layers).

360 In agreement with previous studies Σ_{Π} takes both positive and negative values in S1 and S2
 361 (Fig. 8) with a sign change for $k \gtrsim 2\text{-}3 \times 10^{-4} \text{ rad m}^{-1}$ which corresponds to wavelengths of the
 362 order of 25 km, well resolved at $\Delta x = 1 \text{ km}$. Positive values are located at high wavenumbers and
 363 reflect the EKE leakage from the balanced flow toward smaller scales and dissipation. Negative
 364 values at low wavenumbers correspond to the well-known inverse cascade found in rotating strat-
 365 ified flows (Charney 1971). Our focus is on the forward cascade and some issues complicate the
 366 interpretation of this inverse cascade in our simulations (limited statistical robustness and limited
 367 domain size in the zonal direction) but we note that the magnitude of the latter is about 40 times
 368 larger than that of the former.

369 For the forward cascade, the largest values for Σ_{Π} are found in S1 ($\sim 4 \times 10^{-2} \text{ mW m}^{-2}$) while
 370 high wavenumber Σ_{Π} are indistinguishable from 0 in S3 (not shown). In S2 Σ_{Π} is positive over
 371 roughly the same range as in S1 but with a peak value 7 times smaller. Useful comparisons can
 372 be made between the values of Σ_{Π} in S1 and two other flux terms essential to the energy budget,
 373 1- APE to EKE conversion $\langle \overline{w'b'} \rangle$, which is the primary source of EKE in the simulations, and
 374 2- the amount of energy F_I injected by the restoring terms (see Sec. 2). In practice APE input
 375 through buoyancy F_I^b strongly dominates over KE input through velocity restoring (see table 1).
 376 F_I^b is computed as in Molemaker et al. (2010), *i.e.*, we do not make use of the quasi-geostrophic
 377 approximation to compute APE.

378 The main energy route as it emerges from this analysis is as follows (see table 1): the forcing
 379 provides large amounts of APE in the upper ocean, most of which (0.72 mW m^{-2}) is converted
 380 into KE in the submeso and mesoscale range. The forward energy cascade at submesoscale only
 381 participates marginally to the redistribution and dissipation of that energy with a flux that is less
 382 than 5% of the KE input. A much larger upscale flux takes care of bringing injected energy at
 383 horizontal and vertical scales large enough that bottom friction can act on them. Note that the

384 maximum intensity of the upscale flux can be larger than the total conversion term owing to net
 385 fluxes of pressure work into the 0-200 m layer². Integrated vertically down to the bottom at
 386 $z = -h^{(\max)}$ though we have verified that $-\min(\Sigma_{\Pi}^{h^{(\max)}}) \lesssim \langle \overline{w'b'} \rangle$ (see Table 1). Note also that
 387 the intensity of the full depth forward cascade $\max(\Sigma_{\Pi}^{h^{(\max)}})$ is an even smaller fraction of the full
 388 depth APE release, of the order of 1 %.

389 Another interesting remark concerns the respective roles played by the inverse and forward
 390 cascades in fluxing the additional KE energy input $\langle w'b' \rangle$ present in S1 compared to S2, which
 391 is $\approx 0.5 \text{ mW m}^{-2}$. Most of it is being dealt with by the inverse energy cascade (whose increase
 392 from S2 to S1 is slightly more than 0.5 mW m^{-2} as a plausible consequence of changes in fluxes
 393 of pressure work through the $z=-200$ m surface) and not by the forward cascade whose intensity
 394 in S1 is only a small fraction (~ 10 %) of that amount.

395 All these results are not affected by the fact that we include the quiescent northern and southern
 396 edges of the domain in the flux calculations. Estimates over a restricted central area of width 680
 397 km lead to a similar ratio (6 %) between the intensity of the downscale KE transfer and the KE
 398 input. (When computing Σ_{Π} over an area restricted in the meridional direction, we make use of the
 399 1D hanning window to prevent non-periodicity from affecting our calculation. The obtained flux
 400 is then multiplied by a factor 2 to compensate for variance reduction due to the tapering procedure,
 401 as in Capet et al. 2008c).

402 Overall, the downscale KE cascade translated into a local dissipation rate leads to a modest 2
 403 $\times 10^{-10} \text{ W kg}^{-1}$, averaged over the depth range 0-200 m. To put this number into perspective
 404 we can derive a time scale for the decay of mesoscale energy in the depth range 0-200 m through

²The fact that pressure forces are responsible for an upward flux of energy is surprising. We relate this to our mean state restoring procedure which leads to mechanical energy injection directly into the ocean interior. This is in contrast with the energization of the real interior ocean by winds through a downward flux of pressure work (Roquet et al. 2011).

405 the downscale KE route. Vertically integrated KE in this depth range for the mesoscale resolving
406 solution ($\Delta x = 8$ km, see Fig. 5b) is $200 \times 0.07 = 14 \text{ m}^3 \text{ s}^{-2}$. Assuming approximate equipartition
407 of energy we obtain an estimate for mesoscale energy $\sim 28 \text{ m}^3 \text{ s}^{-2}$. This leads to a decay time
408 scale for the mesoscale $\gtrsim 20$ years (in contrast using the maximum intensity of the inverse cascade
409 diagnosed in S1 - 1.6 mW m^{-2} leads to a physically consistent 200 days time scale). This further
410 confirms that the direct KE cascade in S1 is of small magnitude. This is even more true for S2
411 which has comparable levels of mesoscale energy but a downscale KE flux about 7 times smaller
412 than S1.

413 To make sure that our conclusion does not overly depend on the relative efficiency of the large
414 scale energy sink we have performed a sensitivity run $S1_{rd}$ identical to S1 except that the bottom
415 drag coefficient was reduced by a factor 10 ($r_d = 1.5 \times 10^{-4} \text{ m s}^{-1}$). The simulation is analyzed at
416 equilibrium as detailed in Sec. 2c. It is important to realize that reducing bottom drag has profound
417 consequences on the whole energetics, in ways that may not be consistent with the functioning of
418 the real ocean. More intense eddy activity permitted by the reduction of viscous forces leads to a
419 very large increase in release of APE which, in turn, leads to an increase in APE injection because
420 of the type of full depth restoring we use. In the real ocean no external forcing maintains interior
421 buoyancy gradients. Buoyancy restoring in $S1_{rd}$ is responsible for an unrealistic 26 mW/m^2 of
422 domain-average APE injection. And domain average EKE levels near the surface approach 2600
423 $\text{cm}^2 \text{ s}^{-2}$ (1.5 increase compared to S1), which is on the upper limit of what can be locally found
424 in the real ocean (Ducet and Le Traon 2001). Even then, the downscale EKE cascade offers a
425 dissipation pathway to just above 6 % of the APE to EKE conversion (see table 1), *i.e.*, a fraction
426 similar to that found for S1. We tend to see this 6 % figure as an upper bound and will further
427 elaborate on this in the conclusion.

428 **6. Effect of a mixed layer**

429 The simulations analyzed so far have no well-mixed boundary layer. This may be an important
430 limitation. We indeed wonder if a conflict exists between the perturbed motions needed to amplify
431 the Charney mode versus mixed layer instability modes. Essential to our Charney instability is the
432 subsurface layer where Q_y is negative (and IQ_y decreases, see Fig 3a). If a mixed layer occupies a
433 significant fraction of that layer C-BCI growth and the associated turbulent fluxes may be reduced
434 by the growth of mixed layer eddies.

435 The numerical methods we use to perform linear instability analysis do not withstand vanishingly
436 small N^2 in the upper ocean. Thus, we explore the interplay between Charney BCI and
437 mixed layer instability through nonlinear simulations. Specifically, we compute solutions for S1
438 and S2 with a mixed layer artificially created by increasing the vertical diffusion and viscosity
439 coefficients within ~ 65 m from the surface (see Sec. 2b and c for details). These simulations are
440 called $S1_{ml}$ and $S2_{ml}$.

441 Fig. 9 represents the time-averaged vertical buoyancy flux for $S1_{ml}$ and $S2_{ml}$ along with those
442 for S1 and S2 repeated from Fig. 5. The signature of mixed layer baroclinic instability overwhelms
443 the buoyancy flux structure with maxima around the middle of the mixed layer that are 10 times
444 more intense than in S1 and S2. The maximum values we obtain ($\lesssim 5 \times 10^{-8} \text{ m}^2 \text{ s}^{-3}$) are a bit
445 larger than those found in Capet et al. (2008c) ($\sim 1.5 \times 10^{-8} \text{ m}^2 \text{ s}^{-3}$ see their figure 9) but the mean
446 mixed layer depth is also larger, by a factor 2 roughly. General agreement is also found with the
447 typical values of $\langle w'b' \rangle$ in Boccaletti et al. (2007).

448 The comparisons between S1, S2, $S1_{ml}$ and $S2_{ml}$ allows us to gain insight into the interplay be-
449 tween the mixed layer and Charney BCI in weakly stratified regimes. Firstly, it highlights a limit
450 of the Fox-Kemper et al. (2008) parameterization (hereafter FK08) for mixed layer submesoscale

451 effects. FK08 is based on a scaling for the eddy buoyancy flux that only involves the mixed layer
452 depth and the low-passed filtered lateral gradient of buoyancy. Mixed layer depths are identical
453 by construction in $S1_{ml}$ and $S2_{ml}$. Large scale lateral buoyancy gradient are also identical by con-
454 struction and we have verified that this property is passed on to the statistical distribution of frontal
455 intensity in mesoscale resolving ($\Delta x = 8$ km) versions of $S1_{ml}$ and $S2_{ml}$ (not shown). Fox-Kemper
456 et al. (2008) would thus predict identical vertical buoyancy fluxes at submesoscale for simulations
457 $S1_{ml}$ and $S2_{ml}$, whereas they differ by $\approx 20\%$. This demonstrates that the flow and thermohaline
458 structure immediately below the mixed layer can contribute to the submesoscale dynamics of the
459 mixed layer albeit modestly so. A similar conclusion was reached by Ramachandran et al. (2014)
460 who, on the other hand, expose much larger effects of the subsurface on mixed layer buoyancy
461 fluxes. Their sensitivity experiments combine changes in stratification and mean lateral buoyancy
462 gradients below the mixed layer which presumably explains this quantitative difference.

463 A reduction of $\langle \overline{w'b'} \rangle$ is also noticeable below the mixed layer compared to the simulations
464 without mixed layer but it concerns a limited depth range [100-130] m and is modest in amplitude,
465 especially in $S1_{ml}$. In the case of $S2_{ml}$ interaction between mixed layer and subsurface dynam-
466 ics leads to negative $\langle \overline{w'b'} \rangle$ in the subsurface. This is because the subsurface destratification
467 tendency that accompanies the mixed layer restratification (Lapeyre et al. 2006) cannot be com-
468 pensated by other processes (Phillips instability has a deeper center of action). Overall, subsurface
469 vertical buoyancy fluxes remain much stronger in $S1_{ml}$ than in $S2_{ml}$, *i.e.*, the mixed layer eddies do
470 not cancel the C-BCI effects, even for the relatively large mean mixed layer depth we have chosen
471 (65 m).

472 **7. Charney BCI in the real ocean**

473 We now discuss the plausibility that the C-BCI regime exists in the real ocean (just like Phillips-
 474 type instability has been linked with the dynamical regimes in the Southern Ocean, Gulf Stream
 475 ...). General occurrence of C-BCI in the global ocean is studied in Smith (2007) and Tulloch et al.
 476 (2011) but their main focus is on westward flows. Consistent with our numerical experiments, we
 477 focus on C-BCI for near-surface intensified eastward flows. For such flows $\partial_y b$ is negative, $\partial_z U$ is
 478 positive and so is the surface PV sheet gradient term in (1). Satisfying the Charney-Stern condition
 479 for C-BCI implies that the stretching term, $-\partial_z s_b$, be negative below the surface, *i.e.*, that the
 480 isopycnal slope increases when approaching the surface. One particularly favorable situation is
 481 when $\partial_z N^2 < 0$. This can be readily seen by re-expressing the stretching term as:

$$-f\partial_z s_b = +f\partial_z \left(\frac{b_y}{N^2} \right) = -\frac{f}{N^2} \partial_z (-\partial_y b) + \frac{f^2}{N^2} \partial_z U \left(\frac{1}{N^2} \partial_z N^2 \right) \quad (4)$$

482 Due to the nature of frontogenetic processes, ocean fronts tend to be intensified near the surface
 483 so $\partial_z (-\partial_y b)$ is generally positive and we have rearranged the first rhs term to reveal its negative
 484 sign. $\partial_z N^2 < 0$ below the surface implies that the second rhs term is also negative. $\partial_z N^2 < 0$ also
 485 causes the $1/N^2$ and $1/N^4$ factors to increase toward the surface so that stretching is expected to
 486 dominate over β in (1). In S1, stratification weakens upward in the upper 300 m (Fig. 1b) and this
 487 is what explains the presence of C-BCI (the second term in (4) is overwhelmingly responsible for
 488 the negative upper ocean Q_y , not shown).

489 In most parts of the ocean, robust $\partial_z N^2 < 0$ are restricted to a thin “transition layer”, typically
 490 $O(10)$ m, located between the mixed layer base (above which $\partial_z N^2 \sim 0$) and the relatively shallow
 491 core of the pycnocline (*e.g.*, see transition layer thickness statistics in Johnston and Rudnick 2009,
 492 their Fig. 7a). Because the depth range of influence of C-BCI roughly coincides with the layer
 493 where $\partial_z N^2 < 0$ (and $Q_y < 0$) C-BCI will be unimportant when this layer is very thin.

494 A place where one expects to find thick layers with $\partial_z N^2 < 0$ are mode water regions. By def-
495 inition, these regions are characterized by the presence of pycnostads, *i.e.*, , weak upper ocean
496 N^2 and deep N^2 maxima, hence negative $\partial_z N^2$ (and Q_y) over the depth range of the pycnostad.
497 C-BCI can thus be important in such regions. On the other hand, in places and at times where
498 mode waters are actively formed through convection, we expect more energetic instabilities (con-
499 vective/symmetric/mixed layer instability) to dominate upper ocean dynamics over a depth range
500 comparable to that where $\partial_z N^2$ is negative. This leads us to hypothesize that C-BCI may impact
501 mode water dynamics when: 1- winter time convection/subduction has strongly destratified the
502 water column and led to $\partial_z N^2 < 0$ over hundreds of meters; 2- calm weather conditions prevail so
503 the surface mixed layer is relatively shallow, *i.e.*, we are in the type of situation studied numerically
504 in Sec. 6 where C-BCI is important.

505 We now show partial evidence that the spring time southern flank of the Gulf Stream may offer
506 a particular instance where 1- and 2- are satisfied and C-BCI plays a role in the seasonal restrat-
507 ification of the subsurface ocean. Fig. 10 shows monthly mean density structure across the Gulf
508 Stream derived from streamline averaging of all Argo profiles available over the period 2005-2012
509 between longitudes 40°W and 60°W . April and July density sections are represented as well as the
510 integrated meridional PV gradient between two reference profiles located respectively at $y_1 = 1000$
511 km and $y_2 = 1650$ km south of the Gulf stream axis. The month of April was chosen because it
512 corresponds to post wintertime convection conditions with reduced subsurface stratification and
513 thinning mixed layers, of the order of a few tens of meters. Therefore, the vertical buoyancy fluxes
514 (and restratifying tendency) in the upper 100-200 m of the water column are not driven by mixed
515 layer eddies anymore.

516 Wintertime destratification is clearly visible in the depth range 0-200 m while the permanent
517 pool of North Atlantic mode water at greater depths resides, down to about 500m depth. This

518 translates in a monotonic increase of the isopycnal slope roughly above that depth as revealed by
519 the IQ_y profile in Fig. 10. Above 200 m depth s_b and IQ_y change rapidly with depth which is due
520 to the second term in (4) (not shown). Combined to the northward surface density gradient this is
521 a priori conducive to C-BCI and the IQ_y vertical profile is similar to that of S1 (see Fig. 3a), albeit
522 with reduced excursions away from the planetary IQ_y profile.

523 The maximum growth rate curve differs from that found in Sec. 3 for S1 in that it does not exhibit
524 two well-separated instability modes. Nevertheless, the extended range of instability beyond $k=$
525 10^{-4} rad m $^{-1}$ strongly suggest that Charney type BCI instability is regionally important, as the
526 Charney-Stern criterium predicts. The vertical structure of the eigenvector found for $k= 5 \times 10^{-4}$
527 rad m $^{-1}$ (*i.e.*, about 13 km wavelength) is also consistent with Charney BCI upper intensification.
528 The maximum growth rate, obtained at that wavenumber reaches 0.04 days $^{-1}$. It is about half that
529 of the most unstable mode in S1 and also half of the growth rate found for a Charney BCI mode in
530 the Gulf Stream region by Smith (2007). Note that, in contrast to Smith (2007), we have restricted
531 ourselves to the zonal mean part of the flow and our growth rate has a regional significance. A
532 more local analysis with y_1 and y_2 chosen closer to each other do not qualitatively change our
533 conclusions but leads to significantly higher maximum growth rates comparable to or stronger
534 than those in Smith (2007).

535 Stratification evolution between April and July is confined in the upper 200 m where it yields a
536 dramatic reduction of the jump between interior and surface potential vorticity (compare left and
537 right columns in Fig. 10). As a result, the IQ_y profile is approximately monotonic in the upper \sim
538 200 m and high wavenumber baroclinic instability is shut down in July. In the upper 30-50m we
539 expect air-sea heat exchanges to contribute most of the restratification and PV increase. At greater
540 depths, the role of short-wave radiative fluxes and vertical mixing should be limited and our study
541 suggests that rapid restratification may arise from Charney-type BCI. A dedicated examination of

542 the Oleander data for signs of turbulence intensification by C-BCI could be useful to make progress
543 but C-BCI effects, *e.g.*, on spectral EKE distribution variability, may be subtle and hidden by other
544 processes (Callies and Ferrari 2013).

545 In the vicinity of the north Pacific Subtropical Countercurrent (STCC) the buoyancy field also
546 exhibits positive $\partial_z s_b$ with an equatorward buoyancy gradient. It is therefore consistent with the
547 presence of a Charney baroclinic instability mode (see Fig. 2a in Qiu et al. 2014). As in the Gulf
548 Stream region the time period when this mode can be influential is limited to spring after baroclinic
549 modes associated with ~ 100 m thick wintertime mixed layers have disappeared but subsurface
550 stratification remains weak.

551 In the Southern Ocean, mode water formation regions and intense wintertime destratification
552 also occur along some parts of the ACC. Alongstream heterogeneities and the relative lack of
553 observations there make it more difficult to investigate the existence of C-BCI. C-BCI may also
554 play a role on mesoscale dynamics, *e.g.*, in the vicinity of upper ocean anticyclone which generally
555 have strong fronts and $\partial_z s_b < 0$ in their periphery.

556 **8. Conclusions**

557 Numerous flavors of parallel flow instabilities have been found relevant to explain ocean turbu-
558 lence. The upper ocean is prolific in such instabilities because frontal intensification is particularly
559 efficient and also because atmospheric forcings inject large amounts of available potential energy
560 there. Owing to these specificities, baroclinic instabilities associated with the release of APE in the
561 vicinity of fronts are especially relevant to the upper ocean. This study focuses on the description
562 of an oceanic variant of the Charney baroclinic instability (C-BCI), arising from the joint presence
563 of i) an equatorward buoyancy gradient that extends from the surface into the ocean interior and
564 ii) reduced subsurface stratification, *e.g.*, as produced by wintertime convection or subduction.

565 Background conditions conducive to C-BCI have been widely used in previous process studies of
566 submesoscale flows. C-BCI strengthens near-surface frontal activity with important consequences
567 in terms of turbulent statistics: increased variance of vertical vorticity and velocity, increased
568 vertical turbulent flux of buoyancy which, in turn, implies enhanced nonlinear transfers of KE
569 both upscale and downscale. Dedicated analyses allow us to offer insight into the energetics that
570 underlies submesoscale intensification of flows conducive to C-BCI.

571 The relevance of C-BCI to the real ocean is an important issue that we have explored in a way
572 complementary to Smith (2007) by focusing on eastward flows. Linear stability analysis suggests
573 that regions where seasonal episodes of convection and/or subduction of mode waters creates
574 weakly stratified subsurface conditions will be susceptible to Charney baroclinic instability. A nu-
575 merical sensitivity experiment indicates that mixed layer eddy dynamics does not fundamentally
576 affect the subsurface expression of Charney instability modes. Submesoscale rich realistic sim-
577 ulations of the Gulf Stream region and in particular its southern flank might be useful to further
578 explore Charney instability in a fully realistic context.

579 Notwithstanding the importance of C-BCI in the real ocean the present investigation offers useful
580 theoretical lessons on two subjects, the significance of the downscale energy cascade and the
581 parameterization of eddy induced fluxes of properties in the ocean.

582 *a. Lessons on the intensity of the downscale kinetic energy cascade in the ocean*

583 The possibility that submesoscale allows meso- and large-scale flows to equilibrate through
584 a forward cascade of kinetic energy en route to dissipation has been explored for almost two
585 decades. Theoretical arguments support the breakdown of the QG inverse cascade paradigm (Char-
586 ney 1971) and the existence of the forward route for primitive equations or non-hydrostatic flows
587 (McWilliams et al. 2001; Molemaker et al. 2005; Müller et al. 2005) but existing studies disagree

588 on its strength and overall energetic significance. Idealized studies tend to indicate that it is sig-
589 nificant. Molemaker et al. (2010) demonstrate that the QG and non-hydrostatic solutions of an
590 Eady flow strongly differ in their submesoscale regime, with implications for the spin down and
591 forced-dissipative equilibration of the solutions. As the submesoscale is progressively resolved
592 small scale dissipation decreases dramatically in QG whereas it is maintained at finite levels in
593 non-hydrostatic solutions. In equilibrated solutions about 1/2 (resp. 1/3) of the kinetic (resp.
594 mechanical, *i.e.*, kinetic and potential) energy dissipation involves advective fluxes toward small
595 scales in the submesoscale range. Similar findings and conclusions are obtained by Barkan et al.
596 (2015). In direct numerical simulations for an idealized wind and buoyancy forced periodic flow,
597 they find a vigorous forward EKE cascade associated with frontal instabilities. Dissipation occurs
598 preferentially at small scale in these simulations with a secondary role played by bottom friction,
599 *i.e.*, the dissipation route toward larger scales.

600 In Capet et al. (2008c) and Marchesiello et al. (2011) downscale KE fluxes rapidly vanish below
601 50 m depth (*e.g.*, see Fig. 2 bottom panel in Capet et al. 2008c) and their quantitative importance
602 is limited. For example the intensity of the KE forward cascade diagnosed in Capet et al. (2008c)
603 implies a dissipation of the order of $1.5 \times 10^{-9} \text{ W kg}^{-1}$ in the mixed layer, a value that is typically
604 very small in regard to that induced by air-sea interactions. It is also not very effective in terms of
605 mesoscale energy dissipation because it is so confined into the mixed layer.

606 The present study allows us to place these contradictory results into perspective. Comparison
607 between S1 and S2 demonstrate the major sensitivity of the downscale energy cascade to the upper
608 ocean stratification. For a given large scale buoyancy gradient, baroclinic flows with reduced
609 stratification undergo larger downscale energy cascades. S1 with intense levels of upper ocean
610 KE, a large scale north south buoyancy gradient squared $\sim 1.5 \times 10^{-8} \text{ s}^{-2}$ and a stratification
611 characterized by $N^2 \sim 0.1\text{-}0.2 \text{ s}^{-2}$, on the lower end of what can be found in the mid-latitude

612 upper ocean (Emery et al. 1984), may offer a useful upper bound estimate for the intensity of
613 that cascade. An important conclusion of this study is that even in the favorable situation S1 the
614 downscale advective flux of KE remains a small fraction (≈ 0.05) of the other fluxes involved in
615 the energetics of the system (energy input through the restoring terms mainly as APE, APE to KE
616 conversion, and KE flux toward large scales). Modest sensitivities to, *e.g.*, large scale dissipation
617 intensity through bottom drag may change this number somewhat but do not cast doubt on our
618 general conclusion that the downscale route is of limited significance. Sensitivity to horizontal
619 resolution below $\Delta x = 1$ km would also need to be explored but this is not expected to dramatically
620 affect the intensity of the forward cascade (Capet et al. 2008c). Irrespective of such a sensitivity,
621 our main conclusion on the dependence of the downscale energy flux intensity upon subsurface
622 stratification should hold.

623 In the light of these results (and in agreement with the conclusions of Jouanno et al. 2015) we
624 attribute the substantial downscale cascades present in Molemaker et al. (2010) and Barkan et al.
625 (2015) to unrealistically low N^2 and/or N^2/M^2 . This is evident in Barkan et al. (2015). Isopycnals
626 in their wind and buoyancy forced flow intersect both the bottom and surface over most of the
627 baroclinic zone, which rarely occurs in the open ocean (see their figure 3; their N^2 is 5-10 times
628 weaker than in the real ocean). Likewise, the basic state in Molemaker et al. (2010) has a M^2/N^2
629 dimensional value which is uniform by definition of the Eady flow and equal to 0.2, *i.e.*, much
630 larger than typically found in the real ocean.

631 Our general results are also at odd with the global estimates of the downscale energy flux ob-
632 tained by Brüggemann and Eden (2015). Based on a set of numerical forced-dissipative experi-
633 ments Brüggemann and Eden (2015) establish a relation between the bulk Richardson number of
634 baroclinic flows and the fraction of the APE release $\langle w'b' \rangle$ dissipated at small scale as a conse-
635 quence of the submesoscale energy cascade. Extrapolations based on an eddy permitting realistic

636 global ocean simulation then yields an estimate of small scale dissipation due to submesoscales
637 in the range 0.2-0.5 TW, *i.e.*, a substantial fraction of the energy input to the general circulation.
638 We question the validity of the extrapolation performed by Brüggemann and Eden (2015) because
639 it relies on Eady-type experiments to infer ocean interior downscale energy transfers. By con-
640 struction, surface and bottom surface dynamics is influential at all depths in an Eady flow which
641 makes it a priori ill-suited to explore interior ocean dynamics. It is well known that near-surface
642 and ocean interior significantly differ in their frontogenetic behavior (*e.g.*, MacVean and Woods
643 1980; Klein et al. 1998). Fig. 7 exemplifies these surface-interior differences and confirms un-
644 ambiguously that not all APE releases are equally suited to feed a downscale energy cascade at
645 submesoscale.

646 The reasons why the simulations analyzed in Marino et al. (2015) and Pouquet and Marino
647 (2013) develop a substantial downscale energy cascade in contrast to ours may be due to the
648 specifics of their numerical setting. Indeed, we note that their simulations are for a triperiodic
649 ocean (with no boundaries, hence also no near-surface frontal intensification) devoid of large scale
650 energy sink, subjected to a 3D isotropic stochastic forcing, and energetically unequilibrated.

651 Although the energetic analysis of S1 indicates that the downscale route to dissipation remains
652 limited for the overall equilibration of *realistic* baroclinic flow, the role of such energy transfers in
653 the local equilibration and dissipation of ocean fronts is presumably important as found, *e.g.*, by
654 D’Asaro et al. (2011) and Johnston et al. (2011). Overall though, our study emphasizes the major
655 role played by the inverse kinetic energy cascade even at submesoscale, thereby confirming results
656 from Klein et al. (2008b) and more recently Sasaki et al. (2014).

657 *b. Lessons on limitations of and needs for eddy flux parameterizations*

658 The vertical structure of the APE release $\langle w'b' \rangle$ is a key characteristic of baroclinic instability
659 processes. Models with insufficient resolution to produce baroclinic eddies through baroclinic
660 instability rely on parameterizations to mimic the effects of these eddies in terms of fluxes of
661 properties, including vertical fluxes of buoyancy $\langle w'b' \rangle$. Typically, the Gent and McWilliams
662 (1990) parameterization (hereafter GM90) is used to represent the effects of mesoscale eddies in
663 non-eddy resolving simulations, and with reduced intensity in eddy-permitting models ($\Delta x \gtrsim 20$
664 km). For $\Delta x < 10\text{-}20$ km the processes accounted for by GM are well resolved and GM should
665 be turned off. Mixed layer turbulent motions have much smaller scales than mesoscale eddies so
666 that their effects become well resolved only for $\Delta x \lesssim 1$ km. In simulations at coarser resolution
667 the Fox-Kemper et al. (2008) parameterization (FK08) accounts for vertical fluxes by mixed layer
668 eddies under the key assumption that submesoscale frontal circulations are well confined into the
669 mixed layer.

670 The analysis of multiple $\langle w'b' \rangle$ vertical profiles for different baroclinic flows and numerical
671 resolutions (eddy resolving and submesoscale rich) raises several issues regarding the existing
672 parameterizations (GM90 and FK08) and provides some limited guidance on how to improve
673 them.

674 As previously found by Ramachandran et al. (2014) turbulent motions in the mixed layer and in
675 the interior layer below can couple to produce eddy fluxes which differ from those that would be
676 found if these layers did not interact. In particular, mixed layer and subsurface flows in weakly
677 stratified environments conspire to boost mixed layer restratification. This further pleads for a
678 relaxation of the assumption made in FK08 that the base of the mixed layer behaves like a lid
679 preventing surface-subsurface exchanges.

680 Contrary to common wisdom, our analyses also reveal that subsurface vertical eddy buoyancy
681 fluxes have not necessarily converged in eddy resolving simulations and they can further increase
682 when refining horizontal resolution, at least down to $\Delta x = 1$ km. This occurs when the flow is
683 susceptible to fine-scale instabilities such as the Charney baroclinic instability modes we consid-
684 ered. A preliminary exploration suggests that this is not very common but may affect subduction
685 regions and dynamics that are important to the global ocean and climate functioning.

686 More problematically, our simulations show that deep $\langle w'b' \rangle$ associated with interior Phillips-
687 type baroclinic instability are also enhanced when going from $\Delta x = 8$ km to $\Delta x = 1$ km. We have
688 at present limited insight to offer about why that may be, given that the deep APE release takes
689 place at scales that should be well resolved at $\Delta x = 8$ km. We are also hesitant on the significance
690 of this result. Although the tendency to intensifying interior baroclinic instability with increased
691 resolution may be physical the forcing used in our simulations amplifies this tendency in a way
692 that is not. Indeed, in our solutions energy injection naturally increases as eddies drive the ocean
693 mean state closer to rest (full depth energy injection is 30 % higher at 1km than at 8km, *e.g.*, in
694 solution S3 with only Phillips baroclinic instability). The energetics of the real ocean interior is
695 fundamentally different.

696 Because it results from the coupling between surface dynamics (driven by surface buoyancy
697 gradients) and subsurface dynamics (driven by potential vorticity anomalies present below the
698 surface) the Charney baroclinic instability is a process that we find conceptually interesting when
699 contemplating the parameterization of submesoscale subsurface eddy fluxes. The Charney prob-
700 lem suggests for example that both the background stratification N^2 and its vertical derivative ∂_z
701 N^2 be involved in any parameter sweep exploring the sensitivity of $\langle w'b' \rangle$ to the flow charac-
702 teristics. Unfortunately, no suitable analytical expression exists to relate linear growth rates for
703 Charney BCI to environmental parameters, even when N^2 and the interior PV gradient are con-

704 stant (Pedlosky 1987). Ways to circumvent this issue numerically can certainly be found if the
 705 Charney problem confirms to be a good prototype for near-surface/subsurface baroclinic coupling
 706 and property exchanges.

707 APPENDIX

708 **Construction of initial/reference buoyancy profiles for S1-3**

709 Three northern and southern buoyancy profiles (respectively $b_N(z)$ and $b_S(z)$) are needed to con-
 710 struct the initial/reference states corresponding to S1-3. $b_N(z)$ and $b_S(z)$ are constructed as the
 711 sum of four terms: a small depth-independent background stratification that applies equally to
 712 the northern and southern profiles and guarantees static stability; an exponential buoyancy profile
 713 which enhances near-surface stratification without affecting North-South gradients either; a dis-
 714 torted hyperbolic tangent buoyancy profile responsible for the interior meridional buoyancy gra-
 715 dient and also for a stratification asymmetry between the lower (less stratified) and upper (more
 716 stratified) pycnocline, but with no *surface* meridional buoyancy difference; a hyperbolic tangent
 717 buoyancy profile added to the southern profile only which has its inflection point close to the
 718 surface and is the only source of *surface* North-South buoyancy difference. Precisely we have:

$$\begin{aligned}
 b_{N,S}(z) = & b^{(\min)} + N_b^2(z+h^{(\max)}) + \delta b^s \frac{1}{e} \exp\left(\frac{z^s - z}{z^s}\right) + \frac{1}{2} \delta b_{N,S}^{(1)} \left[1 + \tanh\left(\frac{\mathcal{L}_{N,S}(z) - z_{N,S}^{(1)}}{\delta z_{N,S}^{(1)}}\right) \right] \\
 & + \frac{1}{2 \tanh(1)} \delta b_{N,S}^{(2)} \left[1 + \tanh\left(\frac{z^{(2)} - z}{z^{(2)}}\right) \right] \quad (\text{A1})
 \end{aligned}$$

719 where,

$$\mathcal{L}_{N,S}(z) = z_{N,S}^{(1)} + \left(z - z_{N,S}^{(1)}\right) \left[1 + 0.5 \left(\frac{z - z_{N,S}^{(1)} + |z - z_{N,S}^{(1)}|}{1.3 \delta z_{N,S}^{(1)}} \right)^2 \right]^{0.5},$$

$$\delta b_N^{(1)} = \delta b_S^{(1)} \left[1 + \tanh\left(\frac{\mathcal{L}_S(0) - z_S^{(1)}}{\delta z_S^{(1)}}\right) \right] / \left[1 + \tanh\left(\frac{\mathcal{L}_N(0) - z_N^{(1)}}{\delta z_N^{(1)}}\right) \right], \text{ and}$$

721

$$\delta b_N^{(2)} = 0$$

722 z denotes depth, $h^{(\max)}$ is the ocean depth (4000 m), $b^{(\min)} = 2.775 \times 10^{-1} \text{ m s}^{-2}$, $N_b^2 = 9.8 \times 10^{-8}$
723 s^{-2} and other parameter values depend on jet side and/or configuration case, as listed in table 2.
724 The difference between S1 and S2 arises from the exponential term, absent in S1. S1 and S3 differ
725 because the final term in (A1) is absent in S3.

726 *Acknowledgments.* Most numerical simulations were performed through computing allocations
727 PRACE RA1616 and GENCI GEN1140 on Curie. We acknowledge financial support from Agence
728 Nationale pour la Recherche through ANR project SMOC. ARGO data were collected and made
729 freely available by the Coriolis project and programmes that contribute to it.

730 **References**

- 731 Abernathey, R., J. Marshall, M. Mazloff, and E. Shuckburgh, 2010: Enhancement of mesoscale
732 eddy stirring at steering levels in the southern ocean. *J. Phys. Oceanogr.*, **40**, 170–184.
- 733 Akitomo, K., 2010: Baroclinic instability and submesoscale eddy formation in weakly stratified
734 oceans under cooling. *J. Geophys. Res.*, **115**.
- 735 Arbic, B. K., and G. R. Flierl, 2004: Baroclinically unstable geostrophic turbulence in the limits
736 of strong and weak bottom Ekman friction: Application to midocean eddies. *J. Phys. Oceanogr.*,
737 **34**, 2257–2273.
- 738 Ascani, F., K. Richards, F. E., S. Grant, K. Johnson, Y. Jia, R. Lukas, and D. Karl, 2013: Physical
739 and biological controls of nitrate concentrations in the upper subtropical North Pacific Ocean.
740 *Deep Sea Res., Part II*, **93**, 119–134.

741 Barkan, R., K. B. Winters, and S. G. Llewellyn Smith, 2015: Energy cascades and loss of balance
742 in a reentrant channel forced by wind stress and buoyancy fluxes. *J. Phys. Oceanogr.*, **45**, 272–
743 293.

744 Boccaletti, G., R. Ferrari, and B. Fox-Kemper, 2007: Mixed layer instabilities and restratification.
745 *J. Phys. Oceanogr.*, 2228–2250.

746 Bretherton, F. P., 1966: Critical layer instability in baroclinic flows. *Quart. J. Roy. Meteor. Soc.*,
747 **92**, 325–334.

748 Brüggemann, N., and C. Eden, 2015: Routes to dissipation under different dynamical conditions.
749 *J. Phys. Oceanogr.*, **45**, 2149–2168.

750 Callies, J., and R. Ferrari, 2013: Interpreting energy and tracer spectra of upper-ocean turbulence
751 in the submesoscale range (1–200 km). *J. Phys. Oceanogr.*, **43**, 2456–2474.

752 Callies, J., G. Flierl, R. Ferrari, and B. Fox-Kemper, 2016: The role of mixed-layer instabilities in
753 submesoscale turbulence. *J. Fluid Mech.*, **788**, 5–41.

754 Capet, X., E. J. Campos, and A. M. Paiva, 2008a: Submesoscale activity over the Argentinian
755 shelf. *Geophys. Res. Lett.*, **35**, L15 605.

756 Capet, X., F. Colas, P. Penven, P. Marchesiello, and J. C. McWilliams, 2008b: Eddies in eastern-
757 boundary subtropical upwelling systems. *Ocean Modeling in an Eddy Regime*, M. Hecht,
758 and H. Hasumi, Eds., Geophys. Monog. Ser., Vol. 177, Am. Geophys. Union.

759 Capet, X., J. McWilliams, M. Molemaker, and A. Shchepetkin, 2008c: Mesoscale to submesoscale
760 transition in the california current system. part iii: Energy balance and flux. *J. Phys. Oceanogr.*,
761 **38**, 2256–2269.

- 762 Capet, X., J. C. McWilliams, M. J. Molemaker, and A. Shchepetkin, 2008d: Mesoscale to sub-
763 mesoscale transition in the California Current System. part ii: Frontal processes. *J. Phys.*
764 *Oceanogr.*, **38**, 44–64.
- 765 Charney, J. G., 1947: The dynamics of long waves in a baroclinic westerly current. *J. Met.*, **4**,
766 135–163.
- 767 Charney, J. G., 1971: Geostrophic turbulence. *J. Atmos. Sci.*, **28**, 1087–1095.
- 768 Charney, J. G., and M. E. Stern, 1962: On the stability of internal baroclinic jets in a rotating
769 atmosphere. *J. Atmos. Sci.*, **19**, 159–172.
- 770 D’Asaro, E., C. Lee, I. Rainville, R. Harcourt, and L. Thomas, 2011: Enhanced turbulence and
771 energy dissipation at ocean fronts. *Science*, **15**, 318–322.
- 772 Ducet, N., and P.-Y. Le Traon, 2001: A comparison of surface eddy kinetic energy and reynolds
773 stresses in the gulf stream and the kuroshio current systems from merged topex/poseidon and
774 ers-1/2 altimetric data. *J. Geophys. Res.*, **106**, 16 603–16 622.
- 775 Eady, E. T., 1949: Long waves and cyclone waves. *Tellus A*, **1**.
- 776 Emery, W., W. Lee, and L. Magaard, 1984: Geographic and seasonal distributions of brunt-väisälä
777 frequency and rossby radii in the north pacific and north atlantic. *J. Phys. Oceanogr.*, **14**, 294–
778 317.
- 779 Fox-Kemper, B., and R. Ferrari, 2008: Parameterization of mixed layer eddies. II: Prognosis and
780 impact. *J. Phys. Oceanogr.*, **38**, 1166–1179.
- 781 Fox-Kemper, B., R. Ferrari, and R. Hallberg, 2008: Parameterization of mixed layer eddies. I:
782 Theory and diagnosis. *J. Phys. Oceanogr.*, **38**, 1145–1165.

- 783 Gent, P. R., and J. C. McWilliams, 1990: Isopycnal mixing in ocean circulation models. *J. Phys.*
784 *Oceanogr.*, **20**, 150–155.
- 785 Gill, A. E., J. S. A. Green, and A. J. Simmons, 1974: Energy partition in the large-scale ocean
786 circulation and the production of mid-ocean eddies. *Deep Sea Res.*, **21**, 499–528.
- 787 Giordani, H., and G. Caniaux, 2001: Sensitivity of cyclogenesis to sea surface temperature in the
788 northwestern atlantic. *Mon. Wea. Rev.*, **129**, 1273–1295.
- 789 Johnston, T., D. L. Rudnick, and E. Pallàs-Sanz, 2011: Elevated mixing at a front. *J. Geophys.*
790 *Res.*, **116**.
- 791 Johnston, T. S., and D. L. Rudnick, 2009: Observations of the transition layer. *J. Phys. Oceanogr.*,
792 **39**, 780–797.
- 793 Jouanno, J., X. Capet, G. Madec, P. Klein, and S. Masson, 2015: Dissipation of the energy im-
794 parted by mid-latitude storms in the Southern Ocean. *Ocean Sci.*, submitted.
- 795 Klein, P., B. L. Hua, G. Lapeyre, X. Capet, S. Le Gentil, and H. Sasaki, 2008a: Upper ocean
796 turbulence from high-resolution 3D simulations. *J. Phys. Oceanogr.*, **38**, 1748–1763.
- 797 Klein, P., B. L. Hua, G. Lapeyre, X. Capet, S. Le Gentil, and H. Sasaki, 2008b: Upper ocean
798 turbulence from high-resolution 3D simulations. *J. Phys. Oceanogr.*, **38**, 1748–1763.
- 799 Klein, P., A.-M. Tréguier, and B. L. Hua, 1998: Three-dimensional stirring of thermohaline fronts.
800 *J. Mar. Res.*, **56**, 589–612.
- 801 Lapeyre, G., and P. Klein, 2006: Dynamics of the upper oceanic layers in terms of surface quasi-
802 geostrophy theory. *J. Phys. Oceanogr.*, **36**, 165–176.

803 Lapeyre, G., P. Klein, and B. Hua, 2006: Oceanic restratification forced by surface frontogenesis.
804 *J. Phys. Oceanogr.*, **36**, 1577–1590.

805 Large, W., J. McWilliams, and S. Doney, 1994: Oceanic vertical mixing: A review and a model
806 with a nonlocal boundary layer parameterization. *Rev. Geophys.*, **32**, 363–403.

807 Levy, M., P. Franks, A. P. Martin, and R. P., 2012: Bringing physics to life at the submesoscale.
808 *Geophys. Res. Lett.*, **39**, L14 602.

809 Levy, M., P. Klein, and A. Treguier, 2001: Impact of sub-mesoscale physics on production and
810 subduction of phytoplankton in an oligotrophic regime. *J. Mar. Res.*, **59**, 535–565.

811 Lima, I. D., D. B. Olson, and S. C. Doney, 2002: Biological response to frontal dynamics
812 and mesoscale variability in oligotrophic environments: Biological production and community
813 structure. *J. Geophys. Res.*, **107**, 25–1.

814 MacVean, M., and J. Woods, 1980: Redistribution of scalars during upper ocean frontogenesis: a
815 numerical model. *Quart. J. Roy. Meteor. Soc.*, **106**, 293–311.

816 Mahadevan, A., A. Tandon, and R. Ferrari, 2010: Rapid changes in mixed layer stratification
817 driven by submesoscale instabilities and winds. *J. Geophys. Res.*, **115** (C03017).

818 Marchesiello, P., X. Capet, and C. Menkes, 2011: Submesoscale turbulence in Tropical Instability
819 Waves. *Ocean Model.*, **39**, 31–46.

820 Marino, R., A. Pouquet, and D. Rosenberg, 2015: Resolving the paradox of oceanic large-scale
821 balance and small-scale mixing. *Phys. Rev. Lett.*, **114**, 114 504.

822 McWilliams, J. C., J. Molemaker, and I. Yavneh, 2001: From stirring to mixing of momentum:
823 Cascades from balanced flows to dissipation in the oceanic interior. *Aha' Huliko'a Winter Work-*
824 *shop*, P. Müller Ed.

- 825 Mensa, J. A., Z. Garraffo, A. Griffa, T. M. Özgökmen, A. Haza, and M. Veneziani, 2013: Season-
826 ality of the submesoscale dynamics in the gulf stream region. *Ocean Dynam.*, **63**, 923–941.
- 827 Molemaker, M., J. McWilliams, and X. Capet, 2010: Balanced and unbalanced routes to dissipa-
828 tion in an equilibrated eady flow. *J. Fluid Mech.*, **654**, 35–63.
- 829 Molemaker, M., J. McWilliams, and I. Yavneh, 2005: Baroclinic instability and loss of balance. *J.*
830 *Phys. Oceanogr.*, **35**, 1505–1517.
- 831 Müller, P., J. C. McWilliams, and M. J. Molemaker, 2005: Routes to dissipation in the ocean:
832 The 2D/3D turbulence conundrum. *Marine Turbulence: Theories, Observations and Models*,
833 H. Baumert, J. Simpson, and J. Sundermann, Eds., Cambridge University Press, 397–405.
- 834 Munk, W., L. Armi, K. Fischer, and F. Zachariansen, 2000: Spirals on the sea. *Proc. R. Soc. Lond.*
835 *A*, **456**, 1217–1280.
- 836 Nurser, A., and J. Zhang, 2000: Eddy-induced mixed layer shallowing and mixed layer-
837 thermocline exchange. *J. Geophys. Res.*, **105**, 21 851–21 868.
- 838 Pedlosky, J., 1987: *Geophysical Fluid Dynamics*. Springer-Verlag, 710 pp.
- 839 Pouquet, A., and R. Marino, 2013: Geophysical turbulence and the duality of the energy flow
840 across scales. *Phys. Rev. Lett.*, **111**, 234 501.
- 841 Qiu, B., S. Chen, P. Klein, H. Sasaki, and Y. Sasai, 2014: Seasonal mesoscale and submesoscale
842 eddy variability along the North Pacific Subtropical Countercurrent. *J. Phys. Oceanogr.*, **44** (12),
843 3079–3098.
- 844 Ramachandran, S., A. Tandon, and A. Mahadevan, 2014: Enhancement in vertical fluxes at a front
845 by mesoscale-submesoscale coupling. *J. Geophys. Res.*

846 Rivière, P., A. M. Treguier, and P. Klein, 2004: Effects of bottom friction on nonlinear equilibra-
847 tion of an oceanic baroclinic jet. *J. Phys. Oceanogr.*, **34**, 416–432.

848 Roquet, F., C. Wunsch, and G. Madec, 2011: On the patterns of wind-power input to the ocean
849 circulation. *J. Phys. Oceanogr.*, **41**, 2328–2342.

850 Roulet, G., J. C. McWilliams, X. Capet, and M. J. Molemaker, 2012: Properties of steady
851 geostrophic turbulence with isopycnal outcropping. *J. Phys. Oceanogr.*, **42**, 18–38.

852 Sasaki, H., P. Klein, B. Qiu, and Y. Sasai, 2014: Impact of oceanic-scale interactions on the
853 seasonal modulation of ocean dynamics by the atmosphere. *Nat. Commun.*, **5**.

854 Shchepetkin, A., and J. C. McWilliams, 1998: Quasi-monotone advection schemes based on ex-
855 plicit locally adaptive dissipation. *Mon. Wea. Rev.*, **126**, 1541–1580.

856 Shchepetkin, A., and J. C. McWilliams, 2005: The Regional Oceanic Modeling System: A split-
857 explicit, free-surface, topography-following-coordinate ocean model. *Ocean Model.*, **9**, 347–
858 404.

859 Shchepetkin, A., and J. C. McWilliams, 2009: Correction and commentary for "Ocean forecasting
860 in terrain-following coordinates: Formulation and skill assessment of the regional ocean mod-
861 eling system" by Haidvogel et al, *J. Comp. Phys.* 227, pp. 3595-3624. *J. Comput. Phys.*, **228**,
862 8985–9000.

863 Skyllingstad, E. D., and R. Samelson, 2012: Baroclinic frontal instabilities and turbulent mixing
864 in the surface boundary layer. part i: Unforced simulations. *J. Phys. Oceanogr.*, **42**, 1701–1716.

865 Smith, K., 2007: The geography of linear baroclinic instability in earth's oceans. *J. Mar. Res.*, **65**,
866 655–683.

- 867 Spall, S., and K. Richards, 2000: A numerical model of mesoscale frontal instabilities and plank-
868 ton dynamics - i. model formulation and initial experiments. *Deep Sea Res.*, **47 (I)**, 1261–1301.
- 869 Thomas, L., and R. Ferrari, 2008: Friction, frontogenesis, and the stratification of the surface
870 mixed layer. *J. Phys. Oceanogr.*, **38**, 2501–2518.
- 871 Thomas, L., and J. Taylor, 2010: Reduction of the usable wind-work on the general circulation by
872 forced symmetric. *Geophys. Res. Lett.*, **37**, L18 606.
- 873 Tulloch, R., J. Marshall, C. Hill, and S. Smith, 2011: Scales, growth rates and spectral fluxes of
874 baroclinic instability in the ocean. *J. Phys. Oceanogr.*, **41**, 1057–1076.

875 **LIST OF TABLES**

876 **Table 1.** Maximum value of S1 advective KE flux Σ_{Π} reached in the submesoscale
 877 range; maximum upscale flux intensity reached in the mesoscale range; total
 878 energy input F_I through zonal restoring (on velocities and buoyancy); contribu-
 879 tion to this energy input due to buoyancy restoring F_I^b alone; conversion from
 880 APE to EKE ($\langle \overline{w'b'} \rangle$) and rate of change δ_t EKE accounting for EKE drift
 881 between the solution end state and initial state. Numbers in the first row (resp.
 882 second row) are for the reference S1 experiment (resp. the sensitivity exper-
 883 iment with reduced bottom drag S1_{rd}). In each box numbers before and after
 884 the '/' separator refer to integrated values from surface to 200 m and bottom
 885 respectively. All numbers are in mW m⁻². 43

886 **Table 2.** Parameter values for the initial and reference states of the three setups S1-3.
 887 Within each box, "/" separates northern and southern values. Only S2 values
 888 are filled when a parameter does not vary across setups. $\delta b_N^{(1)}$ (in bold) is
 889 calculated so that the first hyperbolic tangent term in (A1) does not contribute
 890 to the North-South buoyancy difference at the surface. 44

891 TABLE 1. Maximum value of S1 advective KE flux Σ_{Π} reached in the submesoscale range; maximum upscale
892 flux intensity reached in the mesoscale range; total energy input F_I through zonal restoring (on velocities and
893 buoyancy); contribution to this energy input due to buoyancy restoring F_I^b alone; conversion from APE to EKE
894 ($\langle \overline{w'b'} \rangle$) and rate of change δ_t EKE accounting for EKE drift between the solution end state and initial state.
895 Numbers in the first row (resp. second row) are for the reference S1 experiment (resp. the sensitivity experiment
896 with reduced bottom drag $S1_{rd}$). In each box numbers before and after the '/' separator refer to integrated values
897 from surface to 200 m and bottom respectively. All numbers are in mW m^{-2} .

$\max(\Sigma_{\Pi})$	$-\min(\Sigma_{\Pi})$	F_I	F_I^b	$\langle \overline{w'b'} \rangle$	δ_t EKE
0.04 / 0.055	1.7 / 3.6	0.82 / 8.4	0.78 / 8.2	0.72 / 5.9	-0.05 / -0.03
0.12 / 0.85	4.6 / 12	2.7 / 22	3.1 / 26	2.0 / 25	+0.06 / 1.38

898 TABLE 2. Parameter values for the initial and reference states of the three setups S1-3. Within each box, ”
 899 / ” separates northern and southern values. Only S2 values are filled when a parameter does not vary across
 900 setups. $\delta b_N^{(1)}$ (in bold) is calculated so that the first hyperbolic tangent term in (A1) does not contribute to the
 901 North-South buoyancy difference at the surface.

	S1	S2	S3
δb^s	0	7.1×10^{-3}	0
z^s	0	-110	0
$\delta b_{N/S}^1$		1.413×10^{-2} / 1.4×10^{-2}	
$z_{N/S}^{(1)}$		-400 / -1000	
$\delta z_{N,S}^{(1)}$		300 / 700	
$\delta \rho_{N,S}^{(2)}$	0 / 1.5	0 / 1.5	0 / 0
$z^{(2)}$	-300	-300	×

902 **LIST OF FIGURES**

903 **Fig. 1.** Northern and southern vertical profiles of buoyancy (left), Brunt-Väisälä frequency (center)
904 and lateral buoyancy gradient modulus (right) at the center of the domain . Continuous (resp.
905 dashed and dotted) lines correspond to S1 (resp. S2 and S3) profiles. Northern profiles for
906 S1 and S3 are identical. Lateral buoyancy gradients for S1 and S2 are also identical. 47

907 **Fig. 2.** Cross-section of initial/reference buoyancy b_{ref} for S1 (top), S2 (middle) and S3 (right).
908 Contour interval is $2.5 \times 10^{-3} \text{ m s}^{-2}$ 48

909 **Fig. 3.** Left (a,c,e): IQ_y vertical profiles for the initial (black) and mean equilibrated (gray) state of
910 S1 (a), S2 (c) and S3 (e). S1 and S2 surface values of IQ_y accounting for the Dirac contri-
911 bution are shown with asterisks. Note the discontinuity associated with these contributions.
912 Extrema of IQ_y profiles for the initial state are shown with open circles. The contribution of
913 planetary vorticity alone is also shown (dashed line). Right (b,d,f): Growth rate of infinitesimal
914 perturbation as a function of wavenumber for S1 (b), S2 (d) and S3 (f). Growth rate
915 maxima are indicated with a plus sign. Vertical profiles of the corresponding eigenvector's
916 modulus are shown between -2000 m depth and the surface (insets). Note the surface trapping
917 of the shortest mode in the case of S1 (dashed line, black for the reference state, gray
918 for the ROMS mean state). 49

919 **Fig. 4.** Surface (a-c, d-f) and 110 m depth (g-i) vertical vorticity (normalized by the Coriolis fre-
920 quency f) in S1 (top), S2 (middle) and S3 (bottom). Vertical velocity at 110 m is also shown
921 (right, j-l, in m/day). All panels correspond to simulations with horizontal resolution $\Delta x = 1$
922 km except surface vorticity panels a-c which are for $\Delta x = 8$ km. All panels represent instan-
923 taneous fields at $t=180$ days. Because no surface intensification is present in S2 vorticity at
924 surface and 110 m are virtually identical, hence the similarity between panels f) and i). 50

925 **Fig. 5.** Vertical profiles of EKE (a,b), w^{rms} (c,d), $\langle \overline{w'b'} \rangle$ (e,f) and frontogenetic tendency due to
926 horizontal advection F_{sh} (g,h) for S1 (solid black), S2 (solid gray) and S3 (dashed) for $\Delta x =$
927 1km (left panels) and 8km (right panels). Estimation uncertainty is indicated with markers
928 (crosses for S1, + for S2 and open circles for S3). It is computed for each domain average
929 variable \bar{X} as $\pm 1/\sqrt{n} X^{std}$ where we suppose that we only have 12 independent realizations,
930 hence $n=12$ (see Section 2.4.) 51

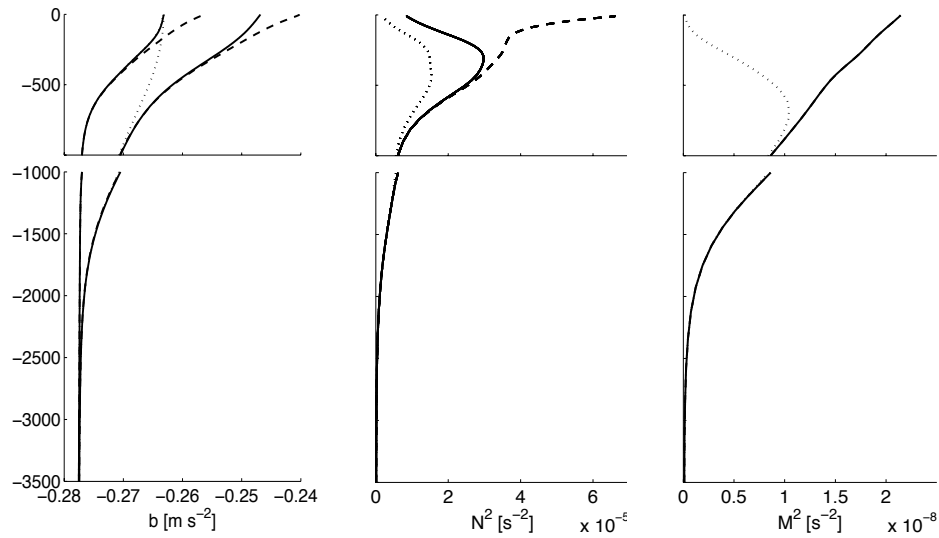
931 **Fig. 6.** Time averaged KE spectra for the horizontal velocity \mathbf{u}_h surface fluctuations as a function of
932 horizontal wavenumber magnitude, $k = |\mathbf{k}_h|$, *i.e.*, the 2D spectrum is azimuthally integrated
933 in k shells. Spectra for S1 (black), S2 (dark gray) and S3 (light gray) at the surface (left) and
934 110m depth (right) are represented. For comparison straight lines indicate -5/3 (dotted) and
935 -3 (dot-dash) spectrum slopes. 52

936 **Fig. 7.** Fraction of the conversion from APE to EKE $C = \langle \overline{w'b'} \rangle$ that is achieved at spatial scales
937 smaller than $k^{sm} = 3 \times 10^{-4} \text{ rad m}^{-1}$, as determined from Fourier spectral analysis (see text
938 and eq (2) for details). Profiles for S1 (resp. S2) are represented with a solid (resp. dashed)
939 line. 53

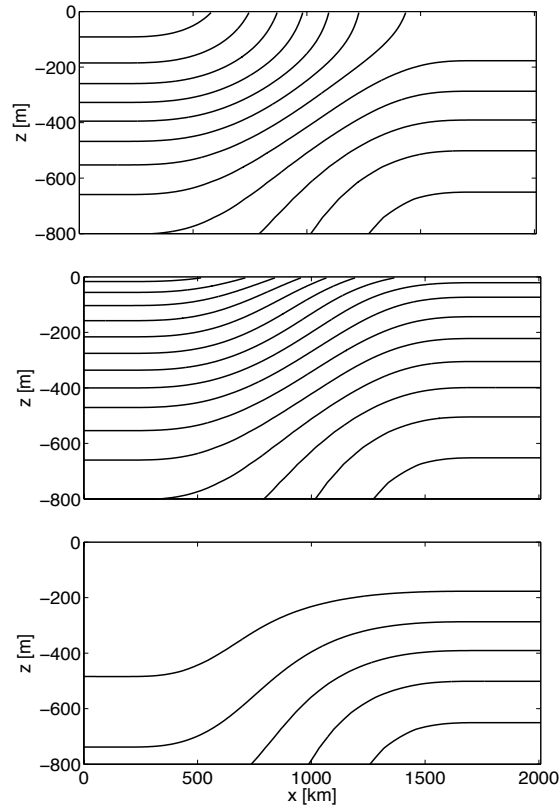
940 **Fig. 8.** Time averaged KE transfer function $\Sigma_{\Pi}(k)$ (in mW m^{-2} , vertical integration over the up-
941 per 200 m) for the solutions S1 (solid black) and S2 (solid gray). S1 uncertainty is also
942 represented as dotted lines based on the assumption that the 360 days run correspond to 12
943 independent realizations. In the inset the vertical scale is refined in the wavenumber range
944 $[10^{-4} - 2 \cdot 10^{-3}] \text{ rad m}^{-1}$ to better appreciate the forward cascade. 54

945 **Fig. 9.** Vertical profiles of $\langle \overline{w'b'} \rangle$ for simulations S1_{ml} (solid black) and S2_{ml} (solid gray). Pro-
 946 files for S1 (dashed black) and S2 (dashed gray) are repeated from Fig. 5. Estimations of
 947 uncertainty are also given as in Fig. 5 based on the assumption that 12 independent realiza-
 948 tions are obtained during our 360 days long simulations. 55

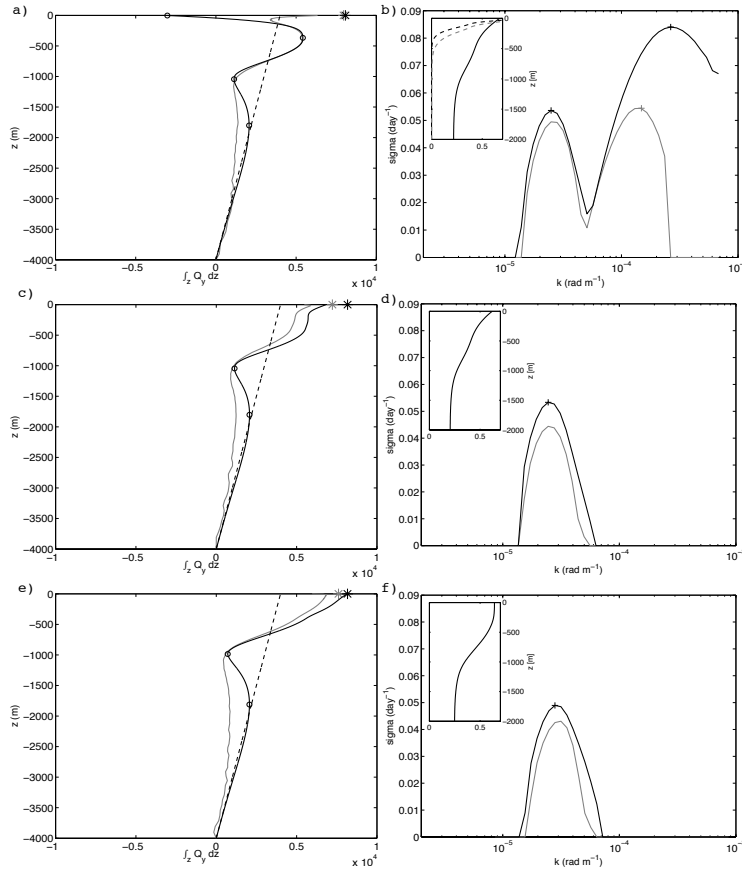
949 **Fig. 10.** Density sections (top, [kg m⁻³]), non dimensional $\int Q_y dz$ (middle) and growth rate [days⁻¹]
 950 derived from all April (left) and July (right) Argo profiles available for the region south of the
 951 Gulf Stream between longitudes 40°W and 60°W. Argo densities are binned using stream-
 952 wise averaging (Abernathey et al. 2010). $\int Q_y dz$ and the unstable characteristics plotted in
 953 (c-f) correspond to the region between located 1000 to 1650 km away from the GS axis
 954 (delimited by white vertical lines in a,b). Symbol definitions are as in Figs. 3. 56



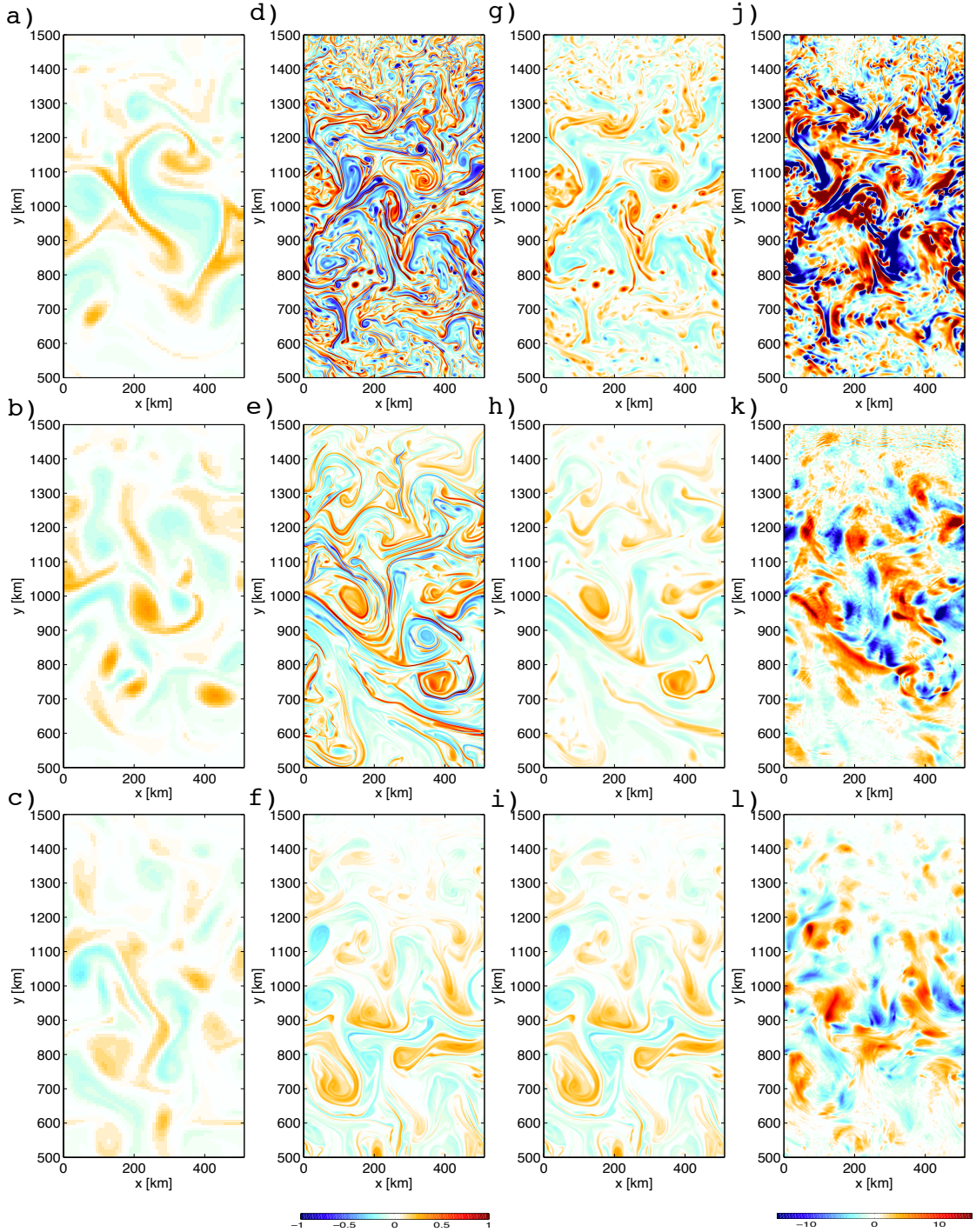
955 FIG. 1. Northern and southern vertical profiles of buoyancy (left), Brunt-Väisälä frequency (center) and
 956 lateral buoyancy gradient modulus (right) at the center of the domain . Continuous (resp. dashed and dotted)
 957 lines correspond to S1 (resp. S2 and S3) profiles. Northern profiles for S1 and S3 are identical. Lateral buoyancy
 958 gradients for S1 and S2 are also identical.



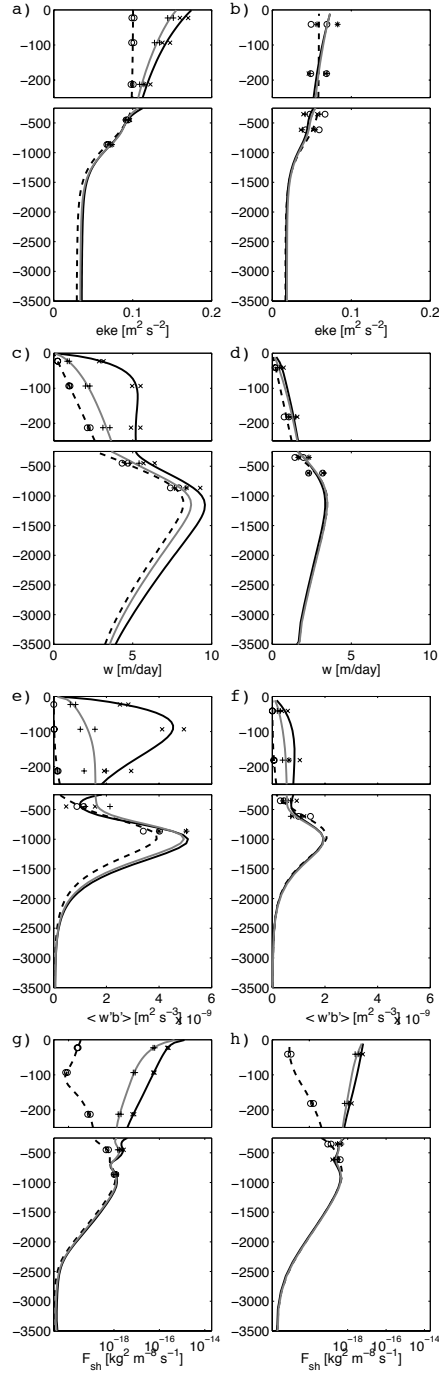
959 FIG. 2. Cross-section of initial/reference buoyancy b_{ref} for S1 (top), S2 (middle) and S3 (right). Contour
 960 interval is $2.5 \times 10^{-3} \text{ m s}^{-2}$.



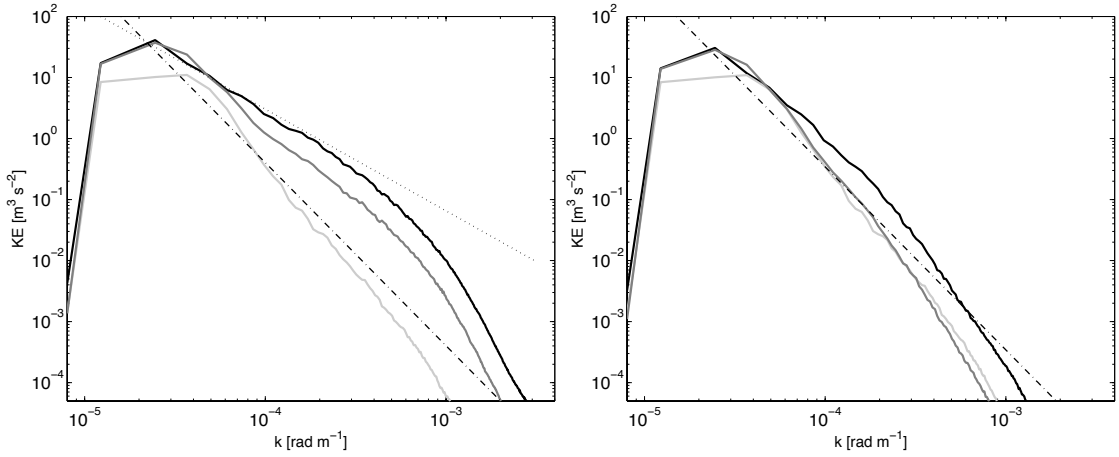
961 FIG. 3. Left (a,c,e): IQ_y vertical profiles for the initial (black) and mean equilibrated (gray) state of S1 (a), S2
 962 (c) and S3 (e). S1 and S2 surface values of IQ_y accounting for the Dirac contribution are shown with asterisks.
 963 Note the discontinuity associated with these contributions. Extrema of IQ_y profiles for the initial state are shown
 964 with open circles. The contribution of planetary vorticity alone is also shown (dashed line). Right (b,d,f):
 965 Growth rate of infinitesimal perturbation as a function of wavenumber for S1 (b), S2 (d) and S3 (f). Growth rate
 966 maxima are indicated with a plus sign. Vertical profiles of the corresponding eigenvector's modulus are shown
 967 between -2000 m depth and the surface (insets). Note the surface trapping of the shortest mode in the case of S1
 968 (dashed line, black for the reference state, gray for the ROMS mean state).



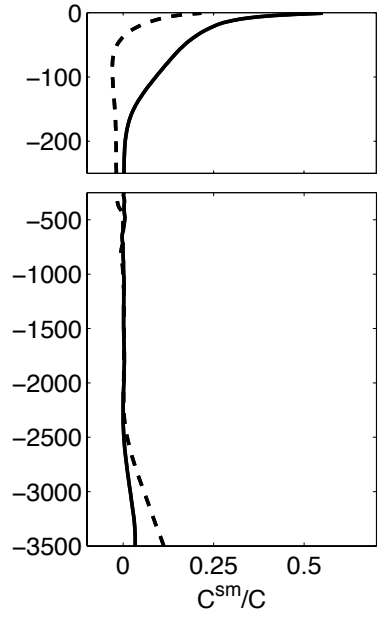
969 FIG. 4. Surface (a-c, d-f) and 110 m depth (g-i) vertical vorticity (normalized by the Coriolis frequency f) in
 970 S1 (top), S2 (middle) and S3 (bottom). Vertical velocity at 110 m is also shown (right, j-l, in m/day). All panels
 971 correspond to simulations with horizontal resolution $\Delta x = 1$ km except surface vorticity panels a-c which are for
 972 $\Delta x = 8$ km. All panels represent instantaneous fields at $t=180$ days. Because no surface intensification is present
 973 in S2 vorticity at surface and 110 m are virtually identical, hence the similarity between panels f) and i).



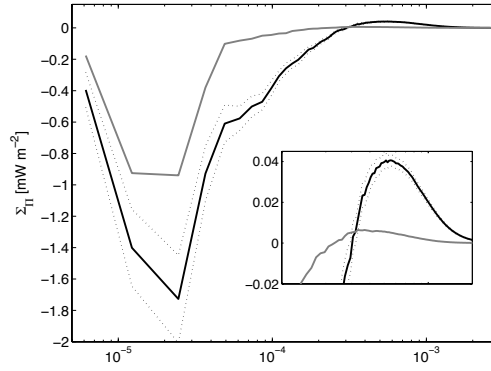
974 FIG. 5. Vertical profiles of EKE (a,b), w^{rms} (c,d), $\langle w'b' \rangle$ (e,f) and frontogenetic tendency due to horizontal
 975 advection F_{sh} (g,h) for S1 (solid black), S2 (solid gray) and S3 (dashed) for $\Delta x = 1\text{km}$ (left panels) and 8km
 976 (right panels). Estimation uncertainty is indicated with markers (crosses for S1, + for S2 and open circles for
 977 S3). It is computed for each domain average variable \bar{X} as $\pm 1/\sqrt{n} X^{std}$ where we suppose that we only have 12
 978 independent realizations, hence $n=12$ (see Section 2.4.)



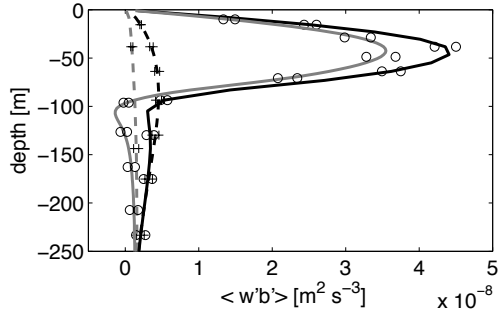
979 FIG. 6. Time averaged KE spectra for the horizontal velocity \mathbf{u}_h surface fluctuations as a function of horizontal
 980 wavenumber magnitude, $k = |\mathbf{k}_h|$, *i.e.*, the 2D spectrum is azimuthally integrated in k shells. Spectra for S1
 981 (black), S2 (dark gray) and S3 (light gray) at the surface (left) and 110m depth (right) are represented. For
 982 comparison straight lines indicate $-5/3$ (dotted) and -3 (dot-dash) spectrum slopes.



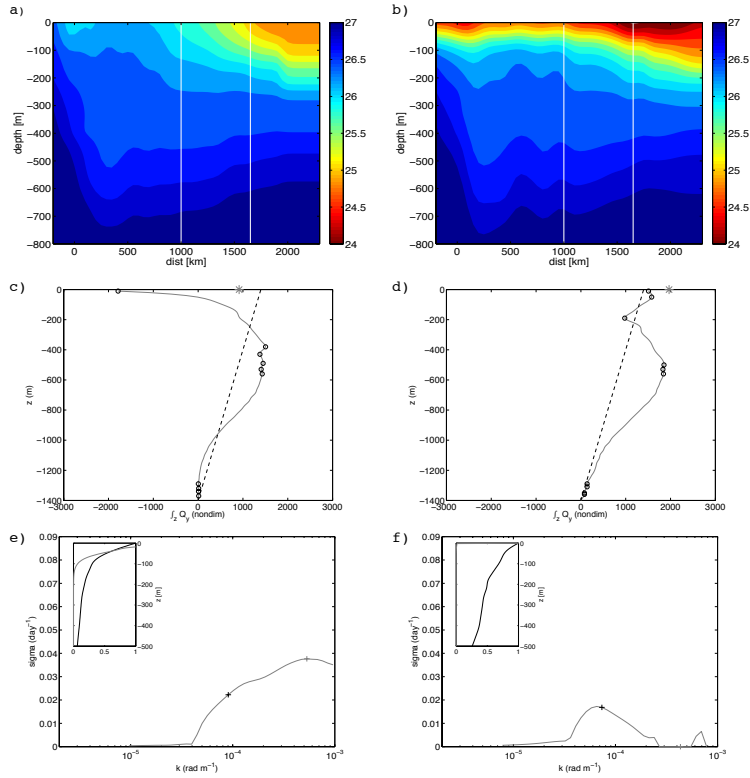
983 FIG. 7. Fraction of the conversion from APE to EKE $C = \overline{w'b'}$ that is achieved at spatial scales smaller
 984 than $k^{sm} = 3 \times 10^{-4} \text{ rad m}^{-1}$, as determined from Fourier spectral analysis (see text and eq (2) for details).
 985 Profiles for S1 (resp. S2) are represented with a solid (resp. dashed) line.



986 FIG. 8. Time averaged KE transfer function $\Sigma_{\Pi}(k)$ (in mW m^{-2} , vertical integration over the upper 200 m)
 987 for the solutions S1 (solid black) and S2 (solid gray). S1 uncertainty is also represented as dotted lines based on
 988 the assumption that the 360 days run correspond to 12 independent realizations. In the inset the vertical scale is
 989 refined in the wavenumber range $[10^{-4} - 2 \cdot 10^{-3}] \text{ rad m}^{-1}$ to better appreciate the forward cascade.



990 FIG. 9. Vertical profiles of $\langle w'b' \rangle$ for simulations $S1_{ml}$ (solid black) and $S2_{ml}$ (solid gray). Profiles for
 991 S1 (dashed black) and S2 (dashed gray) are repeated from Fig. 5. Estimations of uncertainty are also given
 992 as in Fig. 5 based on the assumption that 12 independent realizations are obtained during our 360 days long
 993 simulations.



994 FIG. 10. Density sections (top, [kg m^{-3}]), non dimensional $\int Q_y dz$ (middle) and growth rate [days^{-1}] derived
 995 from all April (left) and July (right) Argo profiles available for the region south of the Gulf Stream between
 996 longitudes 40°W and 60°W . Argo densities are binned using streamwise averaging (Abernathey et al. 2010).
 997 $\int Q_y dz$ and the unstable characteristics plotted in (c-f) correspond to the region between located 1000 to 1650
 998 km away from the GS axis (delimited by white vertical lines in a,b). Symbol definitions are as in Figs. 3.